NUMERICAL SIMULATIONS OF TRIGGERED STAR FORMATION. I. COLLAPSE OF DENSE MOLECULAR CLOUD CORES

HARRI A. T. VANHALA

Department of Terrestrial Magnetism, Carnegie Institution of Washington, 5241 Broad Branch Road NW, Washington, DC 20015-1305; harri@dtm.ciw.edu

AND

A. G. W. CAMERON

Harvard-Smithsonian Center for Astrophysics, 60 Garden Street, Cambridge, MA 02138; acameron@cfa.harvard.edu

Received 1998 March 4; accepted 1998 June 26

ABSTRACT

Results from numerical simulations of shock waves impacting molecular cloud cores are presented. The three-dimensional smoothed particle hydrodynamics code used in the calculations includes effects from a varying adiabatic exponent, molecular, atomic, and dust cooling, as well as magnetic pseudofluid. The molecular cloud cores are assumed to be embedded in background cloud material and to have evolved into their preimpact state under ambipolar diffusion. The shock wave is assumed to be locally plane parallel and steady. The results are sensitive to the thermodynamics employed in the calculations, because it determines the shock structure and the stability of the core. Shocks with velocities in the range of 20–45 km s^{-1} are capable of triggering collapse, while those with lower speeds rarely do. The results also depend on the properties of the preimpact core. Highly evolved cores with high initial densities are easier to trigger into collapse, and they tend to collapse to a single point. Less evolved cores with lower densities and larger radii may fragment during collapse and form binaries.

Subject headings: hydrodynamics — ISM: clouds — shock waves — solar system: formation — stars: formation

1. INTRODUCTION

According to the current theory of star formation, stars are born deep within molecular clouds, when a local density enhancement, a molecular cloud core, grows under the control of ambipolar diffusion to the point where it becomes gravitationally unstable and collapses under its self-gravity (e.g., Shu, Adams, & Lizano 1987). One of the great strengths of this scenario is that it explains why molecular clouds do not collapse as a whole: supported by magnetic fields, only the densest areas of the cloud can collapse directly, while most of the cores must diffuse out their magnetic support on a typical timescale of a few million years (Mouschovias 1989; Shu 1995). Considering the recent observations of how the environment influences the molecular clouds in which stars form (e.g., Hester et al. 1991, 1996; O'Dell, Wen, & Hu 1993; O'Dell & Wen 1994; Thompson et al. 1998), it is uncertain how well the picture of quasistatical growth of molecular cloud cores in quiescent conditions represents the violent conditions in star formation regions. In fact, stars rarely form in isolation, and a significant fraction, possibly even most of the stars, are expected to form in groups and clusters (Lada & Lada 1991). The question is, then, how the conventional picture of molecular cloud core evolution needs to be modified to accommodate the environment in which stars form. How does the evolution of other parts of the molecular cloud influence the development of molecular cloud cores? How do outside effects such as winds and outflows from nearby evolved stars affect the process? In the current standard theory of star formation, these questions remain largely unanswered.

Another argument for the pressing need to understand the effect of environment on star formation comes from the discussion of the origins of the solar system. Studies of primitive meteoritic material have revealed the presence of short-lived radioactivities in the early solar system (see reviews by Cameron 1993; Wasserburg et al. 1994; Podosek & Nichols 1997). The short half-lives of these radionuclides require their introduction to the solar system shortly before their incorporation in the meteoritic material. Despite recent efforts to explain the presence of the radioactivities through in situ production (Clayton & Jin 1995a, 1995b; Shu, Shang, & Lee 1996; Shu et al. 1997), the most likely explanation for their origin is their production through stellar nucleosynthesis in a nearby stellar source, such as a supernova (Cameron et al. 1995; Cameron, Vanhala, & Höflich 1997, hereafter CVH). The timescale for the production of the radioactivities in the stellar interior, their transportation to the molecular cloud core, and their incorporation into the solar system material is 1 million yr or less (Wasserburg et al. 1994, 1995), which is considerably shorter than the magnetic diffusion timescale mentioned above. The apparent problem of timescales can be solved through the hypothesis of the triggered origin of the solar system, which proposes that the transportation mechanism, an interstellar shock wave, also triggered the collapse of the molecular cloud core from which our planetary system was formed (Cameron & Truran 1977; Boss 1995; Cameron et al. 1995; Boss & Foster 1997; CVH). Determining the viability of this proposal requires better understanding of the processes involved in the impact of a shock wave on a molecular cloud core.

There is ample observational evidence for triggered star formation in our Galaxy as well as in extragalactic objects. One of the most striking examples is the NICMOS image of NGC 2264 IRS in the Cone Nebula in Monoceros, where the wind from a B2 star has triggered the formation of six young stellar objects seen at the projected distance of ~4000 AU from the central object (Thompson et al. 1998). Other suggested examples of triggered star formation

include the R association CMa R1, which lies on the edge of an old supernova remnant (Herbst & Assousa 1977), the Trapezium cluster in Orion (Chen et al. 1993), the Upper Scorpius OB association (Walter et al. 1994), and the dust globule ESO 210-6A in the Gum Nebula (Schwartz 1977; Graham & Elias 1983; Graham & Heyer 1989). On a grander scale, interactions between galaxies often compress preexisting molecular clouds or make them collide with each other, in this manner triggering massive star formation (e.g., Higdon & Wallin 1997). Yet another example is the radio galaxy NGC 5128 (Cen A), where a radio jet impacts an adjacent cloud and appears to have triggered star formation (Graham 1998). Clearly, triggered star formation is an important feature of stellar evolution on all scales, from the formation of individual stars to massive starbursts in interacting galaxies. Even though the mechanisms behind the triggering of these various objects may be different, the basic idea of the phenomenon is the same: molecular cloud matter is compressed by an outside agent to the point of collapse.

Elmegreen (1998) discussed various ways in which star formation may be triggered. In the "globule squeezing" scenario, a shock wave compresses a preexisting molecular cloud core and causes it to collapse. In the "collect and collapse" scheme, interstellar matter is accumulated into dense ridges or shells that collapse into dense cores. And finally, cloud collisions may trigger star formation in the interacting parts of the clouds. In the current work, we concentrate on the triggered collapse of preexisting molecular cloud cores. Despite the growing body of evidence for the prevalence of triggered star formation, there have been few studies discussing the details of the process. Numerical simulations are required to study the impact of interstellar shock waves on molecular cloud cores, and it has been only recently that sufficient computational power has become available for a full-scale attack on the problem. In the following, we shall briefly describe some of the calculations that relate to the problem under discussion; for a more complete discussion of the calculations of triggered star formation, the reader is referred to the review by Elmegreen (1998).

Most of the previous studies of the interaction between shock waves and molecular clouds have concentrated on high-velocity shocks with velocities of ~ 1000 km s^{-1} (e.g., Krebs & Hillebrandt 1983). These calculations show that the clouds are usually torn apart by the Rayleigh-Taylor (RT) and Kelvin-Helmholtz (KH) instabilities that result from the interaction between the shock front and the cloud (Różyczka & Tenorio-Tagle 1987; Stone & Norman 1992; Klein, McKee, & Colella 1994, hereafter KMC; Xu & Stone 1995), although it is possible that strong magnetic fields may be able to prevent the clouds from being destroyed (Mac Low et al. 1994). Even if the clouds do survive the impact, they are not compressed to the point of collapse by the fast shock waves (Bedogni & Woodward 1990).

Studies of shocks with lower velocities have produced more favorable results. Calculations of clouds compressed by spiral-arm shock fronts have shown that even though the cloud is strongly distorted by the instabilities, it may be able to survive the interaction and become gravitationally unstable (Woodward 1976). More recently, the probability of shock-triggered collapse has been directly examined by Boss (1995) and Foster & Boss (1996, hereafter FB96; 1997). Boss (1995) investigated the interaction of relatively slow

(≤ 25 km s^{-1}) shock waves with centrally condensed, low-mass (~ 1 $M_\odot$) molecular cloud cores. He found that the combined effect of the cloud's self-gravity and isothermality led to the gravitational collapse of the cloud on a timescale considerably smaller than that required for the shredding of the cloud by RT and KH instabilities. The compression was found to be especially effective with high postshock temperatures. Roughly half of the impinging material was injected into the system, resulting in about 0.01 $M_\odot$ of material mixed into the collapsing protostellar core.

FB96 and Foster & Boss (1997) examined the induced collapse of self-gravitating molecular cloud cores impacted by winds emanating from supernovae or AGB stars or by protostellar outflows. They found that the result of the impact depended on the value of the incident momentum of the shock wave. The critical momentum, which divided the cases that induced collapse from those that did not, was found to scale as the mass of the cloud times its sound speed and was 0.2 $M_\odot$ km s^{-1} for the standard 10 K cloud. The results were also found to be sensitive to the thermodynamics employed in the calculations. A shock with an adiabatic exponent of $\gamma = 5/3$ was found to result in the destruction of the cloud, while $\gamma = 1$ pushed the core into collapse. They interpreted this result as the difference between fast shocks (> 100 km s^{-1}), which destroy the principal cooling agents, leading to the $\gamma = 5/3$ case and cloud destruction, and slow shocks, which do not destroy their cooling agents and so effectively maintain a constant temperature. In the collapsing case, about 10%–20% of incident shock wave material was injected into the collapsing core.

The calculations described above indicate that the scenario of triggered star formation appears to be viable, but they also demonstrate the need for calculations that include detailed thermodynamical considerations. In the current work, the problem is investigated by studying the impact of shock waves on molecular cloud cores through numerical simulations using a three-dimensional smoothed particle hydrodynamics (SPH) code. In order to address the questions raised by the results described above, realistic thermodynamics are employed in the current calculations. Rather than assigning a single value to the adiabatic exponent γ, it is allowed to vary naturally as a function of density and temperature. Judging from the previous results on triggered collapse, this is expected to have an important effect on the outcome of the interaction between the shock wave and the molecular cloud core, and in the calculations presented here, this expectation is confirmed.

In § 2, we shall describe the code used in the calculations, which is based on the standard formulation of the SPH method. In § 3 we present the results of our simulations of moderate-velocity shock waves impacting well-evolved molecular cloud cores. In § 4 the implications and validity of these results are discussed, and in § 5 we summarize the results.

2. THE SIMULATION METHOD

2.1. Description of the Simulation Code

The viability of triggered star formation must be examined through numerical simulations. In the work described here, the SPH method is used to study the impact of an interstellar shock wave on a molecular cloud core. The basic idea of SPH is to divide the hydrodynamical flow into

a set of individual particles that overlap. Properties of the gas at any given point in space can then be calculated as particle sums. We employ the standard formulation of the method (Benz 1990; Monaghan 1992), which translates the basic hydrodynamic expressions for the equation of continuity, the momentum equation, and the energy equation,

$$\frac{\partial \rho}{\partial t} + \nabla \cdot (\rho v) = 0 \; , \tag{1}$$

$$\frac{dv}{dt} = \frac{\partial v}{\partial t} + (v \cdot \nabla)v = -\frac{\nabla P}{\rho} - \nabla \phi \; , \tag{2}$$

$$\frac{du}{dt} = \frac{\partial u}{\partial t} + (v \cdot \nabla)u = -\frac{P}{\rho} \nabla \cdot v - \frac{\Lambda}{\rho} \; , \tag{3}$$

to their SPH numerical counterparts

$$\rho_i = \sum_{j=1}^{N} m_j W(|r_i - r_j|, h) \; , \tag{4}$$

$$\frac{dv_i}{dt} = -\sum_{j=1}^{N} \left[m_j \left(\frac{P_i}{\rho_i^2} + \frac{P_j}{\rho_j^2} + \Pi_{ij} \right) \right. $$
$$\left. \times \nabla_i W(|r_i - r_j|, h) \right] - (\nabla \phi)_i \; , \tag{5}$$

$$\frac{du_i}{dt} = \frac{1}{2} \sum_{j=1}^{N} \left[m_j \left(\frac{P_i}{\rho_i^2} + \frac{P_j}{\rho_j^2} + \Pi_{ij} \right)(v_i - v_j) \right. $$
$$\left. \cdot \nabla_i W(|r_i - r_j|, h) \right] - \frac{\Lambda_i}{\rho_i} \; . \tag{6}$$

In the equations above, ρ denotes density, t time, v velocity, P pressure, $\nabla \phi$ gravitational force, m mass, u the specific internal energy, Π the artificial viscosity, $W(|r_i - r_j|, h)$ the interpolating kernel, and Λ the cooling function. In the SPH formulation, the equations are written for the particle i located at position r_i. The calculations are then carried over all the other particles j, with the summation index running from 1 to N, the total number of particles.

In SPH, the equation of continuity is replaced by equation (4), which calculates density as a sum of particle masses. The continuity equation is satisfied automatically, provided the masses of the particles are constant and none are lost during the computation. Pressure can be calculated from the equation of state using density and temperature; for a description of the equation of state used in the current calculations, see § 2.2. The cooling function will be discussed in § 2.3. Gravitational force can be calculated from the Poisson equation

$$\Delta \phi = \frac{1}{r^2} \frac{d}{dr} \left(r^2 \frac{d\phi}{dr} \right) = 4\pi G \rho \; , \tag{7}$$

which in the SPH form can be written as

$$-(\nabla \phi)_i = -G \sum_{j=1}^{N} \frac{M(|r_i - r_j|)}{|r_i - r_j|^2} \frac{(r_i - r_j)}{|r_i - r_j|} \; , \tag{8}$$

where

$$M(|r_i - r_j|) = 4\pi \int_0^{|r_i - r_j|} u^2 W(u, h) du \; . \tag{9}$$

In practice, the summation of equation (8) over all the particles is too time consuming. Instead, hierarchical trees are used in the calculations (Benz et al. 1990). The resulting time consumed in computing gravity then scales as $N \log N$ instead of the N^2 of direct summation.

Function $W(|r_i - r_j|, h)$, the interpolating kernel lying at the heart of the SPH method, was chosen to be the spline-based,

$$W^{3D}(|r_i - r_j|, h) = \frac{1}{\pi h^3}$$
$$\times \begin{cases} 1 - \frac{3}{2}v^2 + \frac{3}{4}v^3 \; , & \text{if } 0 \le v \le 1 \\ \frac{1}{4}(2 - v)^3 \; , & \text{if } 1 \le v \le 2 \; , \\ 0 \; , & \text{otherwise} \end{cases} \tag{10}$$

where h is the smoothing length determining the number of closest neighbors included in the summations and $v = |r_i - r_j|/h$. The value of h was varied using

$$\frac{dh}{dt} = \frac{1}{3} h \nabla \cdot v \tag{11}$$

in order to keep the number of neighbors between 25 and 60.

Artificial viscosity, which is needed to treat the shocks accurately, is included through the artificial viscous pressure term

$$\Pi_{ij} = \begin{cases} (-\alpha c_{ij} \mu_{ij} + \beta \mu_{ij}^2)/\rho_{ij} \; , & \text{if } (v_i - v_j) \cdot (r_i - r_j) \le 0 \\ 0 \; , & \text{otherwise} \end{cases} , \tag{12}$$

where α and β are free parameters and c is the sound speed. Note that $c_{ij} = 0.5(c_i + c_j)$ and $\rho_{ij} = 0.5(\rho_i + \rho_j)$ in order to ensure momentum conservation and

$$\mu_{ij} = \frac{h(v_i - v_j) \cdot (r_i - r_j)}{|r_i - r_j|^2 + \epsilon h^2} \tag{13}$$

is an estimate of the velocity divergence at particle i because of the presence of particle j. The term ϵh^2 is added to avoid divergence for small $|r_i - r_j|$. In the calculations presented here, α was set to 1.5 and β to 3.0.

Our code is based on the extensively tested three-dimensional version developed by W. Benz. For a more detailed description of the code as well as the tests to which it has been subjected, the reader is referred to the papers by Benz and coworkers (e.g., Benz et al. 1990). The modifications made to accommodate the specifics of the current problem are described in the following sections.

2.2. *Equation of State*

Previous calculations of the interaction between shock waves and molecular clouds have demonstrated the need for careful consideration of thermodynamics. In the current calculations the equation of state is solved following Höflich, Müller, & Khokhlov (1993) and Höflich, Khokhlov, & Wheeler (1995) and references therein. Assuming local thermodynamic equilibrium, the ionization balance and ionization energies are solved through the Saha equation within a chemical network of 39 elements and 316 ions. Pressure and specific internal energy can then be calculated at the desired density and temperature, and the derivatives of thermodynamic quantities, such as the thermodynamic exponents, can be derived from these properties. The calcu-

lations assume an equilibrium mix between the ortho and para states of hydrogen. This assumption is quite uncertain and is discussed further below.

Figure 1 shows the adiabatic exponent $\gamma[(d \log P/d \log \rho)_{\mathrm{ad}}]$ as a function of temperature at a few typical molecular cloud densities. The value of γ falls below the stability line of $\gamma = 4/3$ when molecular hydrogen is excited and dissociated, when neutral hydrogen is being ionized, and when helium is being singly and doubly ionized. At low temperatures the behavior of γ does not depend strongly on gas density. However, the dips in γ associated with the dissociation of hydrogen (marked in Fig. 1 with II) and CO (III) molecules, as well as the ionization of hydrogen and helium (IV, V, VI), take place at higher temperatures as the density increases. The shift of the CO dissociation feature moves slower than the molecular hydrogen dissociation feature, and by panel d the two have merged. Our results for the adiabatic exponent agree well with the calculations of DeCampli et al. (1978).

2.3. Cooling

The cooling rates used in the calculations take into account molecular cooling, grain cooling, and atomic line cooling and assume local thermodynamic equilibrium and optically thin conditions.

The atomic cooling rates are calculated mainly by fitting data from Osterbrock & O'Dell (1968 and references therein) and Lang (1980 and references therein) with updates to atomic data from Kurucz (1991), the opacity project TOPBASE (Cunto & Mendoza 1992), and various other sources (Seaton 1960; Gayet 1970; Reilman & Manson 1979; Wayman 1982 and references therein; West 1985 and references therein; Swings 1988 and references

therein). If no data are available from experiments or detailed quantum mechanical calculations, the general formula of Burgess & Seaton (1960) is used for the lower levels, which is generally regarded as a good approximation (Peach 1967).

The grain cooling rate is calculated following Hollenbach & McKee (1979) and Ruzmaikina & Ip (1994). The grain temperature is found by balancing the heating gains due to absorption from the interstellar radiation field and collisions with gas molecules (if the gas temperature is higher than the grain temperature) and cooling losses due to thermal emission and collisions with gas molecules (if the gas temperature is lower than the grain temperature). Gas cooling due to collisions with cooler grains ($T_{\mathrm{gas}} > T_{\mathrm{gr}}$) is (Hollenbach & McKee 1979)

$$\Lambda_{\mathrm{gr}} = n n_{\mathrm{gr}} \sigma_{\mathrm{gr}} v_p f 2 k_{\mathrm{B}} (T_{\mathrm{gas}} - T_{\mathrm{gr}}) , \qquad (14)$$

where n is the number density of hydrogen nuclei, n_{gr} is the number density and σ_{gr} the collisional cross section of grains, $v_p = (3 k_{\mathrm{B}} T_{\mathrm{gas}}/m_p)^{1/2}$ is the thermal speed of the proton, r_{gr} is the grain radius, k_{B} is the Boltzmann constant, T_{gas} is the gas temperature, T_{gr} is the grain temperature, m_p is the mass of the proton, and f is a constant with values 1 and 0.37 (cold) or 0.16 and 0.11 (warm) for atomic and molecular gas, respectively.

Molecular cooling follows the general guidelines of Hollenbach & McKee (1979), Flower, Pineau-des-Forets, & Hartquist (1986), and Vanhala (1993). The general form of the cooling rate due to molecules can be written as

$$\Lambda_{\mathrm{mol}} = \sum_J n_J Q_J \sum_{J' \neq J} A_{J,J'} E_{J,J'} , \qquad (15)$$

where the sum is taken over energy levels J, n_J is the number density of molecules at level J, Q_J is the partition
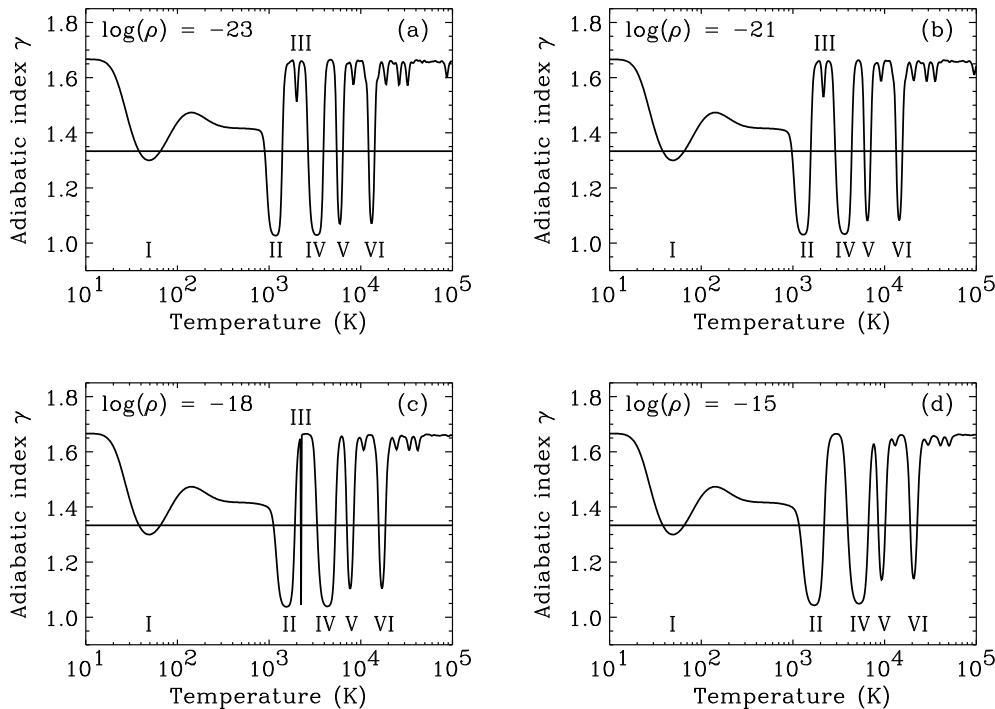

FIG. 1.—Adiabatic exponent γ as a function of temperature at the densities (a) 10^{-23} g cm^{-3}, (b) 10^{-21} g cm^{-3}, (c) 10^{-18} g cm^{-3}, and (d) 10^{-15} g cm^{-3}, assuming an equilibrium mix of the ortho and para states of hydrogen. The major features are marked in the figure by roman numerals I–VI, and they correspond to the excitation (I) and dissociation (II) of hydrogen molecules, the dissociation of CO molecules (III), the ionization of hydrogen atoms (IV), and the single (V) and double (VI) ionization of helium atoms. The smaller wiggles at high temperatures are due to multiple ionizations of C, N, and O atoms. The line at $\gamma = 4/3$ marks the boundary between stable ($\gamma > 4/3$) and unstable ($\gamma < 4/3$) systems.

function of level J, $Q_{tot} = \sum Q_J$, $A_{J,J'}$ is the transition probability from level J to level J', and $E_{J,J'}$ is the corresponding energy difference. The energy of level J can be calculated from (Herzberg 1967)

$$E_J = hc(J(J+1)\{B_v - J(J+1)[D_v - J(J+1)H_v]\}) , \tag{16}$$

where h is the Planck constant, c the speed of light, B_v the mean rotational constant in the vibrational state v, and D_v and H_v are (small) correction terms to the rotational constant. The partition function can be written as (Herzberg 1967)

$$Q_J = f_{op}(2J+1)e^{-E_J/k_BT} , \tag{17}$$

where f_{op} is the ortho-para weighting for H_2: it is set to 1 for CO and is 1 and 3 for the para and ortho states of H_2, respectively. The transition probabilities $A_{J,J'}$ for molecular hydrogen are taken from Turner, Kirby-Docken, & Dalgarno (1977) and for CO from Chackerian & Tipping (1983). When the temperature falls below 10 K, the cooling is turned off.

The molecular cooling rates are calculated prior to the initiation of the simulation run by solving for level populations and transition probabilities. The results are placed in a temperature-density table, which is used as the basis for interpolating the desired cooling rates during the simulation. Since atomic and grain cooling rates can be calculated in a more straightforward manner, they are solved on-line. The cooling rate due to all sources at a typical molecular cloud density is shown in Figure 2. Molecular cooling dominates at temperatures below ~ 2000 K. After the molecules are dissociated, atomic and grain cooling determine the cooling rate.

Optical depth effects have been ignored in our calculations. This is not expected to influence the results until the collapse has proceeded to high densities. Consequently, the collapse is not followed all the way through. Instead, the simulation is stopped when the basic result—whether the impacted core collapses or not—is acquired.

2.4. Magnetic Pseudofluid

Magnetic effects are known to be important in molecular cloud cores. Nonthermal motions observed through line widths of molecular lines are usually attributed to magnetic fields and nonlinear Alfvén waves (Elmegreen 1990). Magnetic fields support the cores against the self-gravity of the gas, and it is only when ambipolar diffusion has sufficiently reduced the flux in the central regions of the core or when an external agent intervenes that gravitational collapse can occur (McKee et al. 1993). Magnetic fields are also known to influence the interaction between molecular clouds and interstellar shock waves (Mac Low et al. 1994).

It is important, then, to consider the effect of magnetic fields in the simulations of the impact of shock waves on molecular cloud cores. In the current calculations the magnetic field is assumed to be fully tangled and frozen into the matter. In this case, magnetic effects can be included in an average sense, as a magnetic pseudofluid (CVH). Adopting this approach for the individual particles yields magnetic energy and pressure terms that vary as the 4/3 power of the density. This has greatly simplified our exploratory calculations.

2.5. Shock Properties

The density jump in a shock front is usually calculated as the ratio $(\gamma+1)/(\gamma-1)$ when a constant γ is used, resulting in a factor 4 in a $\gamma = 5/3$ gas and a factor 7 in a relativistic gas. For a variable γ, however, it is necessary to solve the Rankine-Hugoniot jump equations (e.g., Draine & McKee 1993) directly. In principle, the jump conditions also depend on the field orientation, but in the magnetic pseudofluid approach magnetic effects only enter through energy and pressure terms.

Figures 3, 4, and 5 show the solutions to the shock jump equations for typical molecular cloud conditions in the form of density, temperature, and pressure jumps ρ_1/ρ_0, T_1/T_0, p_1/p_0, where the subscripts 0 and 1 refer to the pre-shock and postshock values of the quantity, respectively. Using the equation-of-state solver described in § 2.2, the density jump (Fig. 3) can approach a factor 40, although the presence of magnetic fields can lower this closer to the conventional values. The high postshock density jump between 10 and 70 km s^{-1} is very important in the context of triggered collapse, since it can act as an efficient battering ram giving high momentum transfer to the encountered molecular cloud core. Figure 4 shows that the postshock temperature is largely unaffected by the presence of magnetic
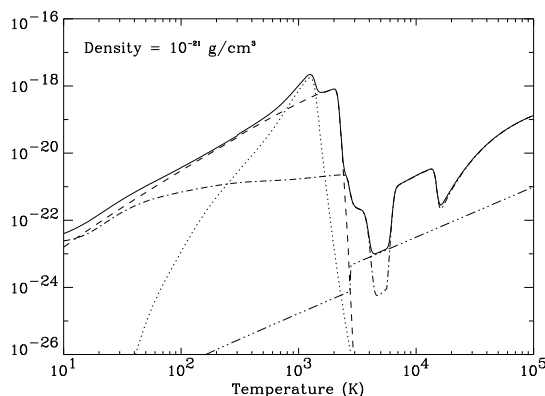

FIG. 2.—Cooling rate Λ as a function of temperature at the density $\rho = 10^{-21}$ g cm^{-3}. The figure shows the total cooling rate (solid line) as well as its major components: cooling due to molecular hydrogen (dotted line), CO (dashed line), dust (dash-triple-dotted line), and atomic cooling (dash-dotted line).
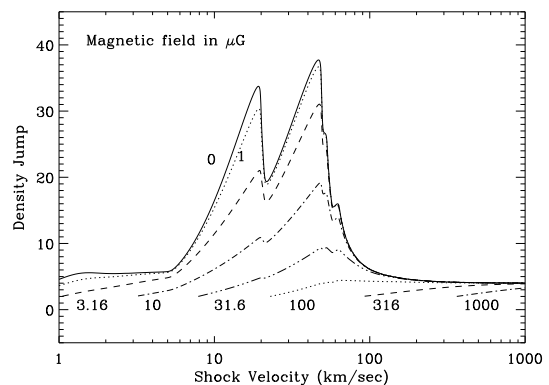

FIG. 3.—Density jump ρ_1/ρ_0 as a function of shock velocity for shocks incident on typical molecular cloud material ($\rho = 10^{-21}$ g cm^{-3}, $T = 10$ K). Curves for a variety of magnetic field strengths are plotted, ranging from 0 to 10^{-3} G. For the higher magnetic fields the curves begin as the density jump just exceeds unity; for lower velocities a shock would not form.
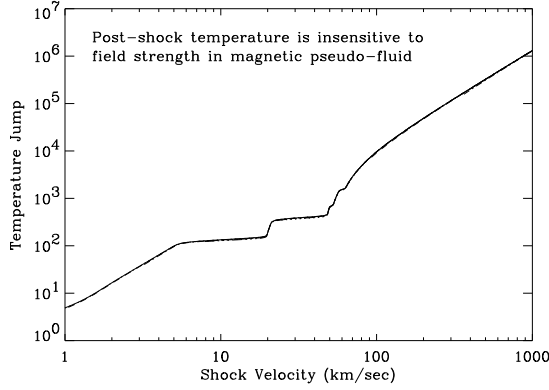
FIG. 4.—Temperature jump T_1/T_0 as a function of shock velocity for shocks incident on typical molecular cloud material ($\rho = 10^{-21}$ g cm^{-3}, $T = 10$ K). Curves for a variety of magnetic field strengths are plotted, ranging from 0 to 10^{-3} G. These curves are almost indistinguishable, showing that the temperature jump is virtually independent of the field strength in the magnetic pseudofluid approach.

field in the magnetic pseudofluid approach. The high post-shock pressure (Fig. 5) is important in exerting additional pressure on the core after the initial impact of the shock front.

2.6. Simulation Space

The simulation space in our calculations consists of a spherically symmetric core embedded in background material with a cylindrical stream of shock particles approaching the core at the desired velocity. Typically, approximately 5000 particles are assigned to the core, while the number of background particles can be twice as large. During the course of the simulation run, more particles are added to the back side of the shock to guarantee a steady flow. Initially, this results in an increasing number of particles, but when the shock flow has passed the core and proceeded beyond the area of interest, particles can be removed from there and recycled as new particles in the postshock flow. In most cases this results in a total number of 20,000–40,000 particles being involved in the simulation. When adding new particles to the system, their positions are randomized to guarantee realistic behavior throughout the simulation space.

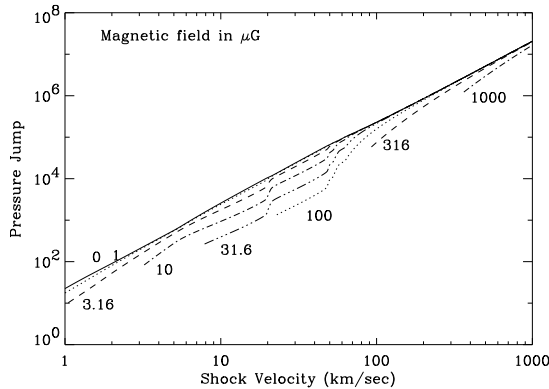The core is assumed to have evolved into its preimpact

FIG. 5.—Pressure jump p_1/p_0 as a function of shock velocity for shocks incident on typical molecular cloud material ($\rho = 10^{-21}$ g cm^{-3}, $T = 10$ K). Curves for a variety of magnetic field strengths are plotted, ranging from 0 to 10^{-3} G. The pressure jump is moderately reduced if a magnetic field is present. The solid line (for 0 magnetic field) shows a small departure from being straight.

state under ambipolar diffusion. This is achieved by making an initial guess at the structure of the core, imposing an artificial force on the system guiding the particles toward a desired density profile, and then allowing the density of the system to change within the evolving gravity field of the configuration and having magnetic flux leak from the central regions of the core into the envelope. While building the core without the force imposed on the particles would be a more realistic way of producing the core, its presence guarantees that the produced density profile follows the desired behavior. This core buildup procedure results in a system where a local density enhancement, the core, smoothly joins to the background gas. The presence of the background material is important for establishing the structure of the shock wave properly before it encounters the core and for assuring realistic behavior of the flow around the core.

The density profile forced on the system during the core buildup is removed before the arrival of the shock wave. This results in the preimpact core being in a state of expansion at the beginning of the simulation, but the expansion motions are negligible compared with the approaching shock flow. Although this approach results in a system that is not in equilibrium, it errs on the side of caution. If the initial conditions were to have any effect on the result of our calculations, they would make collapse more difficult rather than induce it. The results leading to collapse are therefore expected to be true cases of triggered collapse.

Since the simulation space is assumed to be only part of a larger molecular cloud, boundary conditions must be considered. In the current calculations, boundaries are used only for confinement purposes, and nothing interesting is expected to happen there. Boundary effects can therefore be handled through analytical corrections to neighbor sum contributions (Herant 1994). Using the kernel W^{3D} given by equation (10) and defining $\delta = d/h$, where d is the distance of the particle to the boundary, the boundary effects can be calculated from

(1) $0 \leq \delta \leq 1$:

$$\int_{V_{out}} W^{3D} dV = \frac{1}{840(\varrho - \delta)} [186 + 420\varrho - (420 + 588\varrho)\delta$$
$$+ 294\delta^2 + 280\varrho\delta^3 - 70\delta^4 - 126\varrho\delta^6 - 6\delta^7], \quad (18)$$

$$\int_{V_{out}} \nabla W^{3D} dV = \frac{1}{560(\varrho - \delta)^2 h} [124 - 392\varrho^2 + 392\varrho\delta$$
$$+ (-196 + 560\varrho^2)\delta^2 - 560\varrho\delta^3 + (140 - 420\varrho^2)\delta^4$$
$$+ (420\varrho + 168\varrho^2)\delta^5 - (70 + 168\varrho)\delta^6 + 24\delta^7]n. \quad (19)$$

(2) $1 \leq \delta \leq 2$:

$$\int_{V_{out}} W^{3D} dV = \frac{1}{840(\varrho - \delta)} [192 + 448\varrho - (448 + 672\varrho)\delta$$
$$+ 338\delta^2 + 560\varrho\delta^3 - (140 + 420\varrho)\delta^4$$
$$+ (84 + 126\varrho)\delta^5 - (21 + 14\varrho)\delta^6 + 2\delta^7], \quad (20)$$

$$\int_{V_{out}} \nabla W^{3D} dV = \frac{1}{280(\varrho - \delta)^2 h} [64 - 244\varrho^2 + 224\varrho\delta$$
$$+ (-112 + 560\varrho^2)\delta^2 - 560\varrho(1 + \varrho)\delta^3$$
$$+ (140 + 560\varrho + 210\varrho^2)\delta^4$$
$$- (112 + 210\varrho + 28\varrho^2)\delta^5 + (35 + 28\varrho)\delta^6 - 4\delta^7]n, \quad (21)$$

where V_{out} is the volume of the kernel falling outside the boundary, $\mathbf{n}$ the unit vector to the surface, and $\varrho = R/h$, where R is the radius of curvature in the case of a spherical boundary. The particle for which the boundary corrections are calculated is assumed to be on the concave side of the surface.

3. RESULTS

3.1. Comparisons with Previous Simulations

In order to test our three-dimensional SPH code, we studied a few problems similar to those discussed by previous investigations using different simulation methods. The two-dimensional calculations of KMC and Mac Low et al. (1994) have shown the system to be prone to KH and RT instabilities on the contact surface between the core and the shock wave. The resolution of our three-dimensional calculations is lower than in the two-dimensional studies, and to test if our code would be able to observe the instabilities, we ran a few comparison cases with the calculations of KMC. In addition, we were interested in discovering what difference the inclusion of self-gravity would have on the results. We also considered a system similar to the standard case of FB96, which, by studying the impact of slow shock waves on centrally condensed cores, is the best comparison point to our calculations.

3.1.1. Comparison with KMC and Mac Low et al. (1994)

The setup for the simulations trying to reproduce the results of KMC and Mac Low et al. (1994) was chosen in a manner similar to that described by FB96 in § 3.1 of their paper. A spherically symmetric cloud with radius $R_c = 0.022$ pc was placed in the center of the three-dimensional coordinate system. The uniform density cloud ($\rho_c = 1.8 \times 10^{-17}$ g cm^{-3}) was embedded in background medium, the density of which was 1/10 of the cloud density, so that $\chi_{icm} \equiv n_c/n_{icm} = 10$. The temperatures were chosen to be $T_c = 10$ K for the cloud and $T_{icm} = 100$ K for the background material. The simulation space extended to $r_{xy} = 0.066$ pc and -0.18 pc $< z < 0.067$ pc, with the shock wave approaching from the $+z$-direction and starting at $z = 0.044$. The cylindrical edges of the simulation space had reflective boundary conditions, while free inflow/outflow was allowed in the z-direction. The shock wave velocity was set to $v_{shock} = 10$ km s^{-1}, and the equation of state was chosen to be similar to that used in the KMC case, with the value of the adiabatic exponent kept constant at $\gamma = 5/3$.

Figure 6 shows the result from a simulation performed with 18,375 particles. At $t = 2.0 \times 10^4$ yr [$=2.8$ cloud-crushing times t_{cc}, where $t_{cc} \equiv (\chi_{icm})^{1/2} R_c/v_{shock}$], the cloud has been shredded to pieces. Even though the resolution of our calculation is clearly poorer than that of KMC, the results are qualitatively similar in the sense that material is being stripped off at the sides of the cloud and the system is eventually torn apart. Figure 8 of KMC shows a piece of the cloud at the upper right of the picture being torn off and connected by a thin bridge to the main cloud. In our Figure 6, there are two similar features: one on the right-hand side of the main cloud, at roughly $z = -1$ to -2, and the second further down, partially out of the picture. Note that the shock approaches from the opposite directions along the z-axis in Figure 8 of KMC and in our Figure 6. The match between the results is not exact: for example, the pieces torn off from the main cloud are at different locations in the two cases, but the main features are similar and the basic result
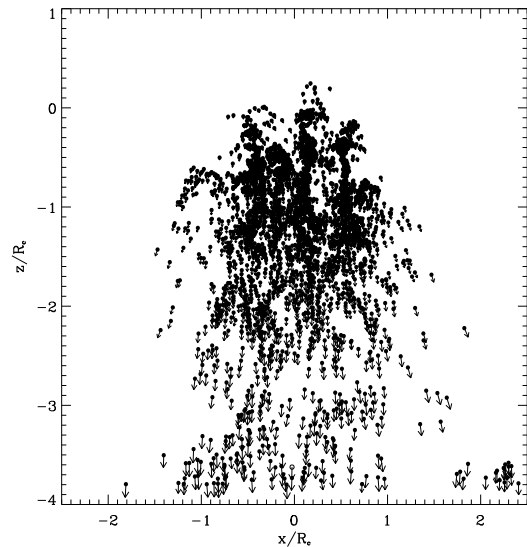

FIG. 6.—Particle positions and velocity vectors at $t = 2.0 \times 10^4$ yr ($=2.8t_{cc}$) in a comparison run with the simulations of KMC. The three-dimensional SPH simulation had 18,375 particles and the adiabatic exponent was $\gamma = 5/3$. The shock wave, traveling with the velocity $v_{shock} = 10$ km s^{-1}, has shredded the cloud through Kelvin-Helmholtz and Rayleigh-Taylor instabilities at the contact surface. The system is shown in the (x, z)-plane with the units in original cloud radii.

is the same. Compared with the resolution study of FB96, our simulation appears to be somewhere between the cases a and b shown in Figure 2 of their paper: the main features are present, but little of the detailed structure can be observed in our Figure 6.

To examine the importance of gravity, we also ran a case with an isothermal equation of state, both with (Figs. 9 and 11) and without (Figs. 7 and 8) self-gravity. The lower value of the adiabatic exponent ($\gamma = 1.00001$) allows for a higher compression: the maximum density in Figure 8 is 1.7 times the maximum density in the $\gamma = 5/3$ case. However, in the
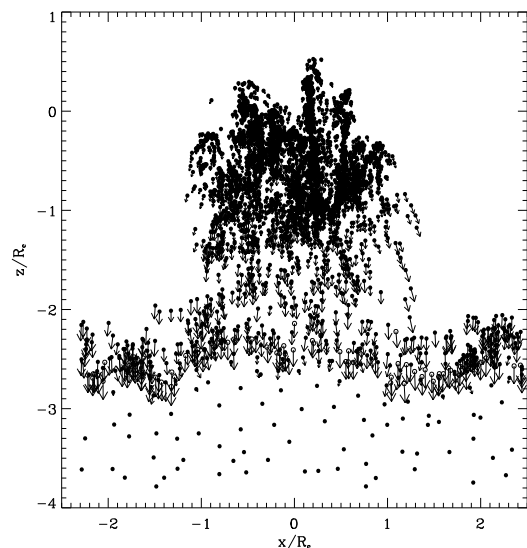

FIG. 7.—Particle positions and velocity vectors at $t = 1.4 \times 10^4$ yr ($=1.9t_{cc}$) in a comparison run with the simulations of KMC. Same as Fig. 6, but the adiabatic exponent $\gamma = 1.00001$. The shock wave particles are denoted by open circles and the cloud and background particles by large dots. The shock has passed through the cloud and is tearing it into fragments.
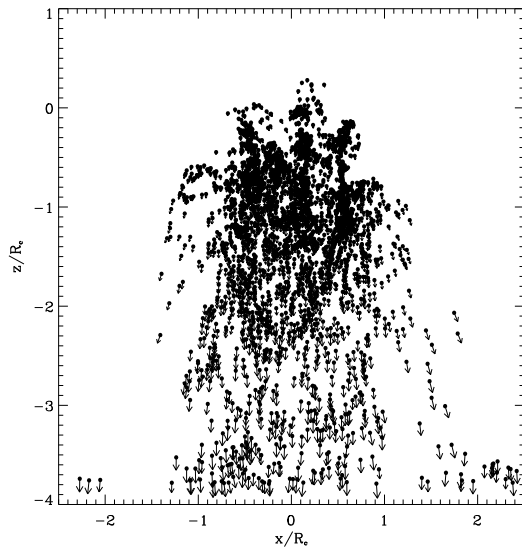
FIG. 8.—Same as Fig. 7, but at $t = 2.0 \times 10^4$ yr ($=2.8t_{cc}$). The cloud is destroyed through Kelvin-Helmholtz and Rayleigh-Taylor instabilities.

FIG. 10.—Density profile along the z-axis near the density maxima in the comparison calculations with the simulations of KMC. The profiles are plotted as a function of distance from the density peak for the cases ignoring (*solid line*) or including (*dotted line*) self-gravity, corresponding to the systems shown in Figs. 7 and 9, respectively. The collapsing case (*dotted line*) has a much higher density peak concentrated on a much smaller area. In the noncollapsing case, the compressed clumps are reexpanding.

absence of self-gravity, the cloud is again destroyed by the instabilities generated in the contact surface between the cloud and the shock wave (Fig. 8), in accordance with the similar case ($\gamma = 1.1$) described by KMC. When self-gravity is included, however, the calculation results in the collapse of the cloud (Fig. 9) by the time $t = 1.4 \times 10^4$ yr. In this case, the cloud is still fragmented by the shock wave, but the fragments are compressed to the point where they can collapse before the instabilities have had a chance to destroy the cloud. Similar behavior was seen by FB96.

The difference between the two cases is illustrated by the density profiles in Figure 10. In the collapsing case, the self-gravity has pulled the clumps of gas together so that the
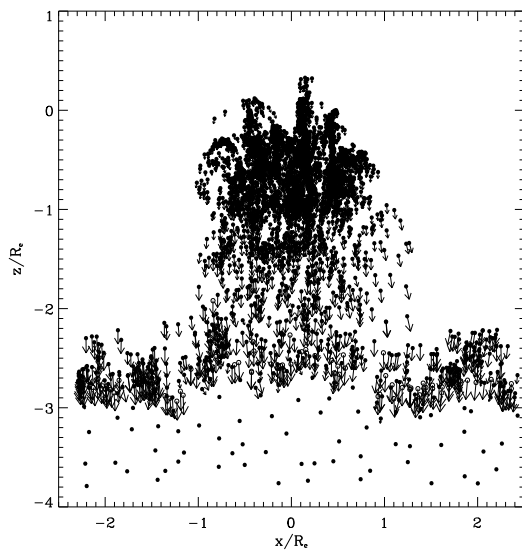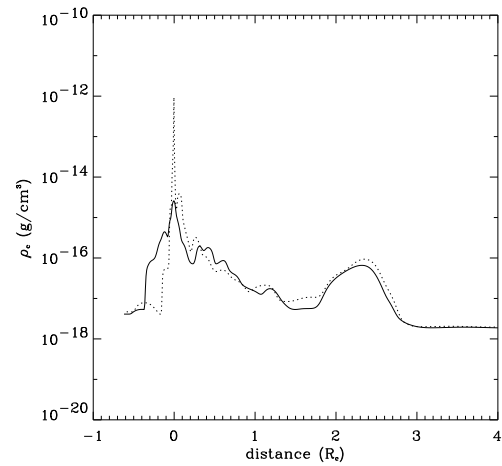
density peak is considerably higher and narrower than in the case where the cloud is eventually torn apart. This also argues for the stability of these clumps of gas against the shock impact, since the disruptive effect of the shock wave depends on the density and radius of the cloud at the compressed state (Nittman, Falle, & Gaskell 1982). In highly condensed small clumps the effect becomes negligible.

Figure 11 shows the system depicted in Figure 9 as a density contour map. The contours trace the filamentary structure of the system, and the relative motions of the

FIG. 9.—Particle positions and velocity vectors at $t = 1.4 \times 10^4$ yr ($=1.9t_{cc}$) in a comparison run with the simulations of KMC. Same as Fig. 7, but with self-gravity. The cloud is severely distorted by the Kelvin-Helmholtz and Rayleigh-Taylor instabilities, but the compression has been sufficient to push the cloud into collapse. The peak density in the collapsing region is 9.94×10^{-10} g cm^{-3}, 5.5×10^7 times the original cloud density.
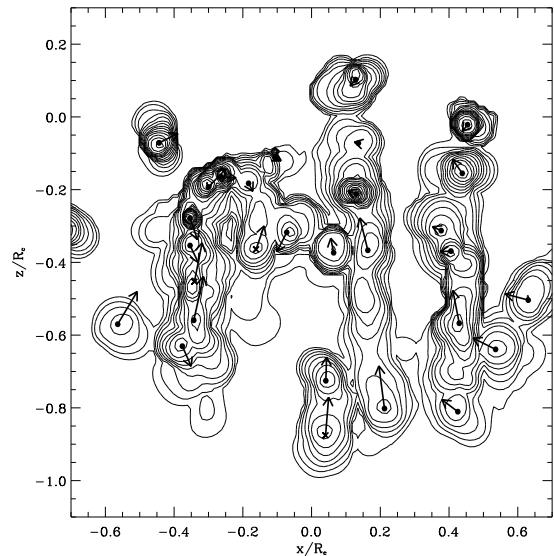

FIG. 11.—Density contours in the KMC comparison run leading to the collapse of the cloud. The contours are spaced in logarithmic intervals from 10^{-16} to 5×10^{-14} g cm^{-3}. The system is shown at $t = 1.4 \times 10^4$ yr, at the same time as Fig. 9. The centers of mass inside each clump of gas are denoted by filled circles or by "X," and the velocity vectors indicate the relative motion of the clumps. The X's correspond to clumps where the first derivative of the moment of inertia is positive, corresponding to expansion, and the filled circles to clumps where the derivative is negative, corresponding to contraction and collapse.

clumps within these filaments indicate that they are converging toward one another. The large number of contracting/collapsing clumps shown by the filled circles indicates that the system is indeed collapsing and not reexpanding as in the cases ignoring self-gravity. The rapid increase in density effectively terminates our calculation at this point both because of the time steps becoming extremely small and because of the resolution of our calculations becoming insufficient as the density increases (see § 4.4). The further evolution of the system cannot therefore be followed.

The conclusion we draw from the comparison runs is that even though the resolution of our simulations is by necessity poorer (because of performing the calculations in three dimensions instead of two), we are able to see the large-scale instabilities responsible for the destruction of the cloud. The basic result of our calculations is essentially the same as in the more detailed two-dimensional simulations. We can therefore proceed to our own calculations confident in the results being realistic, as far as collapse versus destruction of the cloud is concerned. However, one must remember that we are unable to observe the fluid instabilities at the very small scales, which may have an important effect on the detailed behavior of the system (see § 4.2).

3.1.2. Comparison with FB96

The basic configuration of our comparison calculations with the standard case of FB96 follows Figure 3 of their paper, with the obvious exception that our calculations were done in three dimensions. A spherically symmetric cloud was placed at the center of the coordinate system. The masses of the particles within the cloud were varied in order to produce a system similar to that of FB96: a marginally stable Bonnor-Ebert sphere joined smoothly to the surrounding medium. The cloud had a radius of 0.058 pc, temperature of 10 K, and central density of $\rho_c = 6.2 \times 10^{-19}$ g cm^{-3}. The intercloud medium had $T_{icm} = 10$ K and $\rho_{icm} = 7.3 \times 10^{-22}$ g cm^{-3}. The shock wave was represented by a top-hat model, in which the edge of the wave (thickness 0.003 pc) was given the velocity $v_{edge} = 20$ km s^{-1}, density $\rho_{edge} = 7.3 \times 10^{-20}$ g cm^{-3} and temperature $T_{edge} = 10$ K, while the wind behind it had $n_{wind} = 100$ cm^{-3}, $T_{wind} = 10$ K and $v_{wind} = 0$ km s^{-1}. The simulation space extended to $r_{xy} = 0.150$ pc and -0.15 pc $< z < 0.15$ pc, with the shock wave approaching from the $+z$-direction and starting at $z = 0.08$. The cylindrical edges of the simulation space had reflective boundary conditions, while free inflow/outflow was allowed in the z-direction. In accordance with the standard case of FB96, the adiabatic exponent was set to $\gamma = 1.00001$.

Figure 12 shows the basic result from our comparison calculation run with 16,947 particles. Because of slightly higher densities in the shock wave and the intercloud medium, the SPH calculation proceeds somewhat faster than the FB96 standard case, but the basic result is the same. Both calculations lead to the collapse of the core after the leading edge of the shock wave has passed. The postshock material, which initially was at rest, has not moved appreciably during the simulation. On the other hand, some of the shock wave material has penetrated the core and is involved in the collapse. The injection efficiency of our three-dimensional SPH calculations, 19%, is remarkably similar to the 16% of the two-dimensional PPM calculations of Foster & Boss (1997).
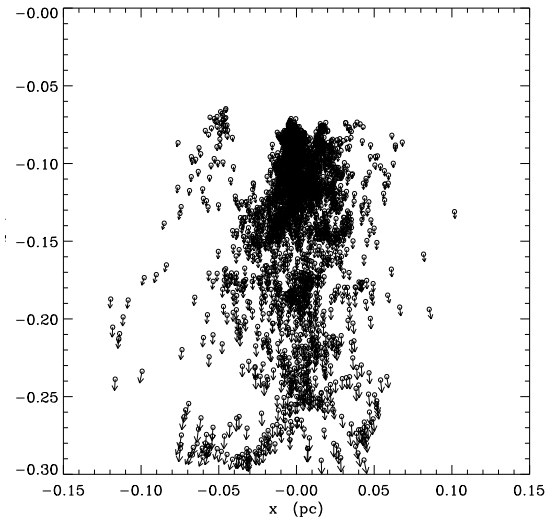

FIG. 12.—Particle positions and velocity vectors at $t = 2.35 \times 10^5$ yr in a comparison run with the simulations of FB96. The three-dimensional SPH simulation had 16,947 particles, and the adiabatic exponent was $\gamma = 1.00001$. The shock wave, traveling with the velocity $v_{shock} = 20$ km s^{-1} has stripped the outer parts of the core and pushed the central regions to collapse. The peak density in the collapsing region, 1.91×10^{-11} g cm^{-3}, is 3.1×10^7 times the original peak density of the core. The shock wave particles are denoted by large dots, and the cloud particles by open circles. The system is shown in the (x, z)-plane with the units in parsecs.

We also ran the standard case with the value of adiabatic exponent set to $\gamma = 5/3$. As expected, the cloud is destroyed (Fig. 13). Some of the impacting material has been reflected from the strong shock at the facing side of the core and pushed back to the postshock material. In this case, wind particles, which initially were at rest, are pushed back toward the origin of the shock wave.

The conclusions we draw from these comparison calculations is that our code can reproduce the two-dimensional results in three dimensions. They also show that we are able to follow the injection of material into the core if it occurs
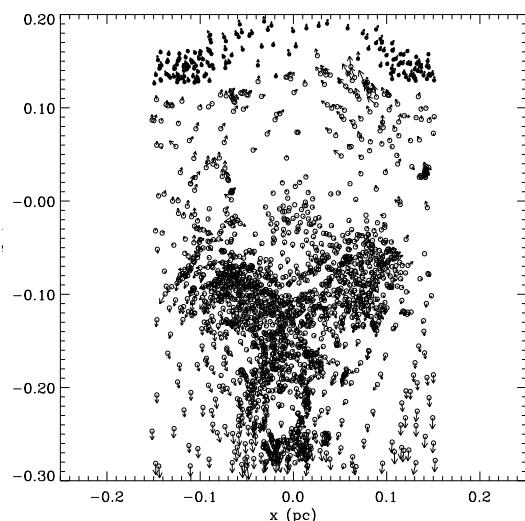

FIG. 13.—Particle positions and velocity vectors at $t = 5.13 \times 10^4$ yr in a comparison run with the shock wave simulations of FB96. Same as Fig. 12, but adiabatic exponent $\gamma = 5/3$. The core bounces from maximum compression and is destroyed. Some of the material is reflected back toward the origin of the shock wave.

through relatively large-scale RT-like fingers (see Boss & Foster 1998).

3.2. *Properties of the Simulation Runs*

Table 1 shows the properties of the simulation runs described in the following sections. The properties of the shock wave are calculated by assuming a locally plane-parallel and steady shock front as described in § 2.5. The shock velocities range from 10 to 50 km s^{-1}. The preimpact cores have radii of ~ 0.1 pc and rise from background cloud density of 10^{-21} g cm^{-3}. The cores have solid body rotation at the rate of 10^{-14} rad s^{-1}, with the rotation axis along the z-axis. Most of the cases considered have relatively low initial masses, with the core masses (the mass within 0.1 pc) ranging from 2.3 to 5 solar masses. The most massive cases, runs I and J, are close to collapse at the beginning of the calculation, with the core mass $M_{core} = 19.9$ solar masses or 90% of the Jeans mass.

The magnetic field strength in the background molecular cloud gas was set to either 0 (runs A–G) or 1 μG (runs H–S). The latter value is toward the lower end of the range measured in molecular clouds, which typically appear to have magnetic field strengths of a few to a few tens of microgauss at the relevant densities (e.g., Crutcher et al. 1993; Troland et al. 1996). We chose this value to keep the field strength at the central parts of the core within a few hundred microgauss. The field strength in the core was determined during the core buildup process through the relation $B_c/B_0 = (\rho_c/\rho_0)^{1/2}$ (Mouschovias 1991). Here B_c and ρ_c are the magnetic field strength and density in the core, and B_0 and ρ_0 are the values of these quantities in the background molecular cloud gas.

The cases ignoring magnetic effects (runs A–G) are included in our study to examine conditions at the limit of negligible magnetic field strengths. The results are not expected to be very different from the magnetic cases. According to Figures 4 and 5, the presence of magnetic fields in the pseudofluid approach does not significantly influence the postshock temperature and the pressure jump. Through their effect on the postshock density (Fig. 3), magnetic fields lower the ram pressure of the shock wave, and

one would expect that triggering collapse will be more difficult to achieve in the magnetic cases. While this is certainly true to a degree, we have found that collapse can also be induced in the presence of magnetic fields. This is because, as will be discussed in § 3.4, collapse is in most cases triggered by the combined effect of the ram pressure of the immediate shock front and the gas pressure of the postshock flow. While the former is reduced in the magnetic cases, the latter is not, and the effect of magnetic fields is not as severe as might otherwise be expected. One must remember, however, that the direction of the magnetic field affects compression: pressure applied along the magnetic field lines can lead to collapse more easily than compression across the field lines. In the magnetic pseudofluid approach the magnetic fields are assumed to be fully tangled and this effect cannot be detected.

3.3. *Interaction between the Shock Wave and the Molecular Cloud Core*

Figure 14 shows the evolution of a typical three-dimensional SPH simulation run (run F) leading into triggered collapse. The initial state (Fig. 14a) is characterized by core temperature of 10 K and central density of 7.35×10^{-17} g cm^{-3}, with the core joining smoothly to the background gas in a bell-shaped density profile. The velocity of the approaching shock front is 25 km s^{-1}, resulting in a density jump of 22 and a postshock temperature of 3650 K.

The interaction of the shock wave with the cloud in our calculations follows the same general path as the behavior of fast shock waves encountering uniform density clouds described by Nittman et al. (1982), Heathcote & Brand (1983), and KMC, among others. While traveling through the molecular cloud, the shock wave sweeps up ambient cloud material. On encountering the core, the shock wave initially flattens it in a planar manner (Fig. 14b) and sends a shock into it. A reflected shock is sent back to the shocked medium, material is diverted to the sides of the core, and the flow settles into a standing bow shock (Fig. 14c) in a manner similar to the flow of the solar wind around the magnetosphere of the Earth.

The facing side of the core is compressed further, while material at its edges is eroded and swept downstream. At the same time, the shock flow around the core begins to converge on the axis behind the cloud, driving a shock into the rear of the cloud (Woodward 1976). According to Nittman et al. (1982), this stage is characterized by a pancake-like structure, because the shocks compressing the sides of the cloud are weaker than those in the front and the back. In our case this phase is rarely reached: the edges of the core erode rapidly during the interaction, and the core is quickly stretched into a filament (Fig. 14d).

The erosion of the core is due to the large-scale instabilities at the contact surface between the hot shocked flow and the cool core material. In the high-velocity shock calculations of KMC this eventually leads to the destruction of the cloud, but in our lower velocity calculations the interaction becomes a competition between the erosion and the self-gravity of the gas. If the combined effect of the ram pressure and the gas pressure from the hot postshock gas is sufficient to compress the head of the filament to densities where self-gravity becomes dominant, the inner parts of the core become gravitationally unstable even while the outer parts continue to erode. This is the case in our example run,

TABLE 1
SIMULATION RUNS: INITIAL CONDITIONS

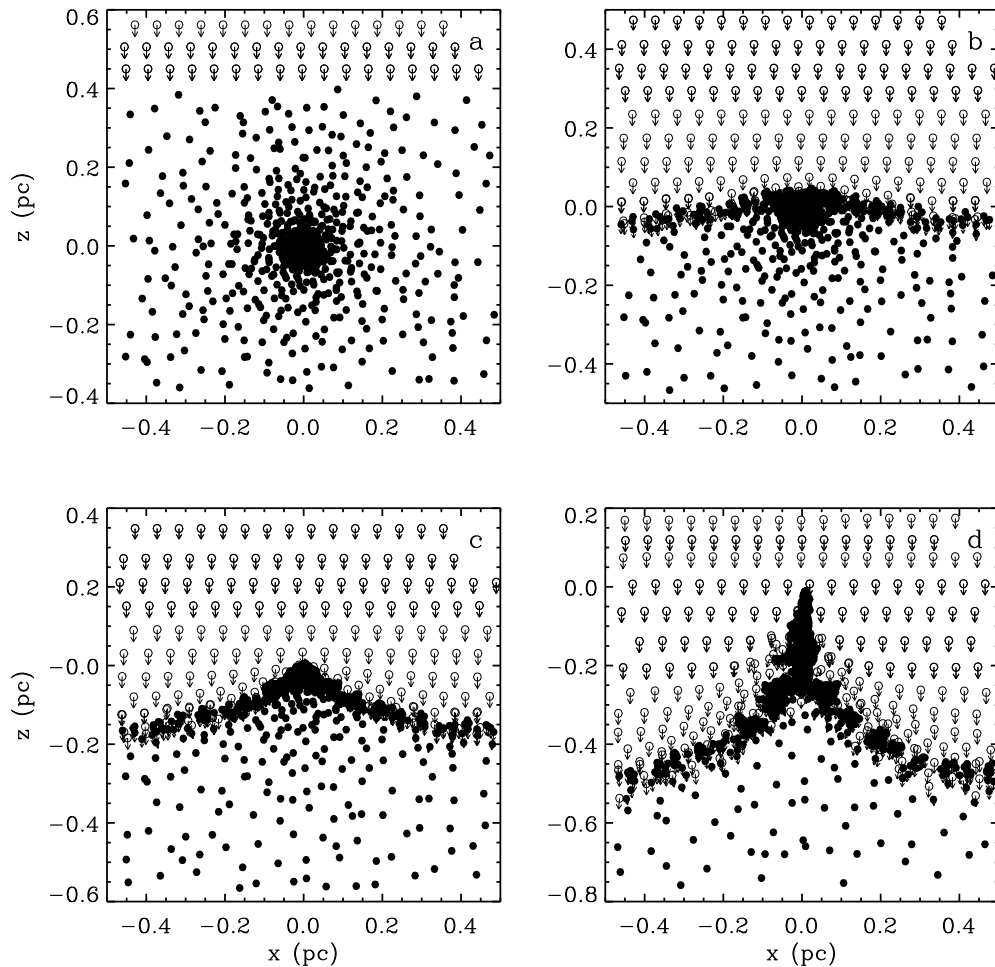| Run	ρ_{max} (g cm^{-3})	Number of Particles	B_{eff} (μG)	v_{sh} (km s^{-1})	Core Mass ($M_\odot$)
A	7.49E$-$19	11501	0	25	9.764
B	7.49E$-$19	11501	0	45	9.764
C	7.83E$-$19	5790	0	25	10.70
D	3.89E$-$18	5880	0	25	14.24
E	9.80E$-$18	11685	0	25	13.66
F	7.35E$-$17	4496	0	25	3.317
G	7.35E$-$17	4496	0	45	3.317
H	6.87E$-$19	3486	1	25	2.342
I	7.49E$-$19	18303	1	10	19.87
J	7.49E$-$19	18303	1	25	19.87
K	7.28E$-$18	4342	1	10	3.735
L	7.28E$-$18	4342	1	19	3.735
M	7.28E$-$18	4342	1	20	3.735
N	7.28E$-$18	4342	1	25	3.735
O	7.28E$-$18	4342	1	50	3.735
P	7.35E$-$18	6417	1	25	3.798
Q	6.87E$-$17	4966	1	19	4.872
R	6.87E$-$17	4966	1	25	4.872
S	8.03E$-$17	7307	1	25	5.260

FIG. 14.—Interaction between the shock wave and the molecular cloud core in a simulation run with 4496 particles in the core and 7772 in the shock wave. The shock wave material is denoted by open circles, and the cloud material by large dots. The initial peak density in the core is 7.35×10^{-17} g cm^{-3}, and the shock velocity is 25 km s^{-1}. The system is shown in the (x, z)-plane with the units in parsecs. The different frames correspond to (a) $t = 0$, (b) 21,000 yr, (c) 27,000 yr, and (d) 42,000 yr.

where the head of the filament collapses while the tail merges into the postshock stream (Fig. 15).

However, if the pressure is not sufficient to cause considerable compression, the instabilities will spread throughout the core, winning the battle against self-gravity, and the core is destroyed in a manner similar to the high-velocity shock calculations. The core is again stretched to a thin filament, but instead of collapsing, the head reexpands both downstream (Woodward 1976) and sideways (Nittman et al. 1982), and the core eventually fragments and is destroyed. Figure 16 shows the end result of a run where the collapse is not achieved (run O). There appears to be little difference between the filaments in Figure 16 and Figure 15, with the exception that in the former case the head is reexpanding from maximum compression while in the latter it is collapsing. Figure 17 shows the gas density as a function of distance from the head of the filament along the z-axis for the two cases shown in Figures 15 and 16. The density peak in the collapsing case is larger by several orders of magnitude, and the larger width of the density peak in the failed collapse case illustrates the reexpansion of the head of the filament.

While the battle between the instabilities and self-gravity is waged within the core, the shock continues to sweep up material from the ambient medium. The shock front may
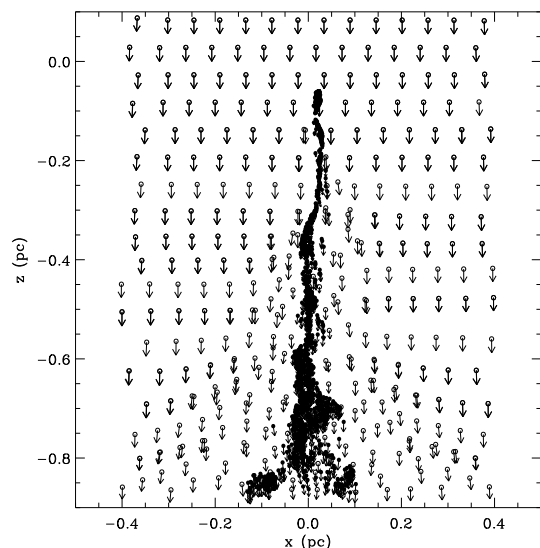

FIG. 15.—End result of a simulation shown in Fig. 14, at $t = 6.96 \times 10^4$ yr. The core has been stretched to a thin filament, the head of which is collapsing. The peak density in the system is 1.72×10^{-11} g cm^{-3}, 2.4×10^6 times the original core density.
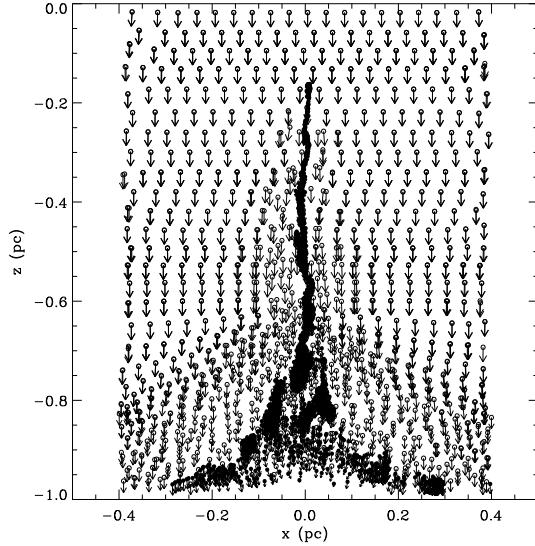
FIG. 16.—Result from a simulation run that does not lead to collapse. The core is stretched to a thin filament, but the temperature in the compressed region does not rise sufficiently to make it unstable against collapse. The system has 7129 particles in the core and 11,287 in the shock wave. The peak density in the system is 3.37×10^{-16} g cm^{-3}, 46 times the original core density. The system is shown in the (x, z)-plane at $t = 75,500$ yr.

FIG. 17.—Density profile along the filament in the cases leading to the collapse (*solid line*) and destruction (*dotted line*) of the cloud. In the failed collapse case the head of the filament is reexpanding. The profiles correspond to Figs. 15 and 16.

then become unstable, fragment, and form self-gravitating clumps of gas. This behavior follows the "collect and collapse" scenario discussed by Elmegreen (1998), and the reader is referred there for a full discussion of the instabilities involved. Traces of this effect may be detectable in Figures 14d and 15, but it must be cautioned that the fragmentation of the shock front into clumps is close to the resolution limit and that it is possible that the fragmentation seen near the tail of the filament is due to numerical effects. However, the question of resolution at the shock front is not expected to influence the case for triggered collapse, since the resolution within the core is much higher than in the ambient gas.

The interaction of the shock wave with the molecular cloud core described above is typical for all cases studied.
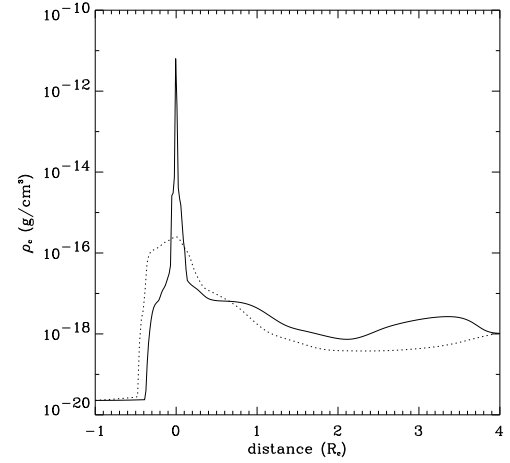
The exact details, such as the shape of the filament (in some cases it may have the appearance of a cone or a thick tube), depend on the initial conditions of the system, but the general behavior follows the path described above. The differences between the cases where triggered collapse occurs and those where it fails are discussed in the next section.

3.4. Requirements for Collapse

Table 2 summarizes the results of our simulations. In general, the behavior of the system can be divided into three regimes according to the velocity of the shock wave. At high speeds the momentum of the shock wave is so high that the cores are shredded apart. The velocity above which shocks are disruptive depends on the initial density of the preimpact core but is typically ~ 45 km s^{-1}. At intermediate speeds (20–45 km s^{-1}), the behavior of the system follows the path described in § 3.3. The shock flow compresses the core considerably and stretches it into a thin filament, the head of which may go into collapse. At low shock speeds (10–20 km s^{-1}), the core is typically compressed by a factor

TABLE 2

SIMULATION RUNS: RESULTS

Run	ρ_{max} (g cm^{-3})	Collapse?	Multiple?	Number of Particles	Time (yr)	Time t_{cc}	$T(\rho_{max})$ (K)	$v_z(\rho_{max})$ (km s^{-1})	f_{core}
A	1.44E−10	Yes	2	36589	6.21E4	1.230	77.43	4.383	0.402
B	2.59E−16	No	No	32669	2.39E4	0.853	10.48	9.408	...
C	2.67E−15	No	No	15891	5.71E4	1.073	10.53	4.873	...
D	1.29E−10	Yes	No	15347	4.84E4	0.789	43.94	2.361	0.295
E	5.68E−09	Yes	No	33071	4.16E4	0.699	428.6	0.740	0.312
F	1.72E−11	Yes	No	12015	5.76E4	1.975	27.79	1.104	0.227
G	3.94E−17	No	No	12040	2.88E4	1.778	10.76	4.351	...
H	7.42E−17	No	No	19650	7.36E4	3.007	10.55	9.047	...
I	2.28E−09	Yes	2	28944	9.74E4	0.579	60.94	0.0649	0.428
J	3.26E−07	Yes	4	35126	6.24E4	1.604	56.77	3.822	0.732
K	4.97E−19	No	No	28357	2.45E5	3.171	10.53	6.291	...
L	4.73E−18	No	No	31450	8.38E4	2.061	22.28	2.882	...
M......	6.24E−18	No	No	29191	1.18E5	3.041	10.58	14.02	...
N	3.66E−15	No	No	27751	5.42E4	1.754	10.48	3.743	...
O	1.38E−17	No	No	29840	3.12E5	20.225	10.52	37.07	...
P	2.65E−16	No	No	25369	8.85E4	3.164	10.45	5.700	...
Q	1.74E−11	Yes	No	15727	3.00E4	0.646	62.73	0.317	0.333
R	8.10E−12	No	No	21397	3.81E4	1.080	10.54	0.000725	...
S	2.26E−14	No	No	21429	3.09E4	0.933	10.52	0.763	...

of a few upon impact, but the ram pressure of the shock front is inadequate to drive the system into collapse. Instead, the core rebounds from the maximum compression and is eventually torn apart. The results of runs A, B, D, E, F, G, J, K, L, M, and O illustrate this conclusion. Runs B, G, and O are torn apart by the high-velocity shocks. Runs A, D, E, F, and J are compressed to the point of collapse. Runs K, L, and M are compressed to 2.8, 4.3, and 4.3 times the original core density, respectively, but they rebound and are eventually torn apart.

The results also depend on the properties of the preimpact core. If the density peak of the molecular cloud core is very high ($> 10^7$ cm^{-3}) or if the cloud is sufficiently massive so that the preimpact core is close to collapse, even low shock velocities may be able to provide the final push. The well-evolved systems can also withstand higher velocities without being shredded apart than lower density cores. The results of runs I and Q illustrate this dependence on the initial state of the system: the cores in these cases collapse even though $v_s = 10$ and 19 km s^{-1}, respectively.

The critical point in determining whether the shock is sufficiently strong to compress the core to the point of collapse is whether the principal coolants, CO and H$_2$, survive in the shock front. At shock velocities higher than 20 km s^{-1}, the molecules are dissociated and the cooling times in the postshock material are longer than the typical flow time past the core. The gas remains hot and provides adequate thermal pressure to act as an efficient battering ram. At lower velocities, the molecules survive, the postshock flow is cooled efficiently, and the ram pressure is inefficient. For the intermediate velocities, the determining factor in whether the compressed core will collapse or bounce back is whether the temperature in the core material rises above a critical value of ≈ 27 K (CVH), at which point the value of the adiabatic exponent γ dips below the collapse neutral value of 4/3 for the first time in typical molecular cloud conditions. In runs A, D, E, F, and J the temperature rises above this value, and they result in the collapse of the core. In runs C, H, N, P, R, and S the temperature remains lower, and the cores do not collapse. Instead, they rebound from maximum compression and are eventually torn apart.

The behavior of the molecular coolants is shown in Figure 18, which plots the abundance of H$_2$ and CO as a function of shock velocity. The amount of H$_2$ in the postshock material decreases steadily as the shock velocity is raised from 7 to 20 km s^{-1} and as the postshock temperature rises above 1000 K. The rapid disappearance of CO at roughly 20 km s^{-1} corresponds to a sudden change in the postshock temperature, which jumps from approximately 1900 to 3200 K in a range of only 2 km s^{-1} in the shock velocity. The effect of these changes on the cooling rate is also shown in Figure 18. After the molecular coolants are dissociated, the cooling rate decreases rapidly. At higher velocities, the postshock temperature continues to rise and atomic cooling governs the cooling rate. The rising part of the cooling curve from 2.5 to 20 km s^{-1} corresponds to the growing postshock density. The shape of the curve at velocities beyond 25 km s^{-1} is determined by the combined effect of the shape of the cooling curve at high temperatures (Fig. 2) and the density jump in the shock front (Fig. 3).

Table 2 also gives the times at which the simulation runs were terminated. These range from 23,900 to 312,000 yr, with a typical value of a few tens of thousands of years. In terms of the cloud-crushing time t_{cc}, these values range from
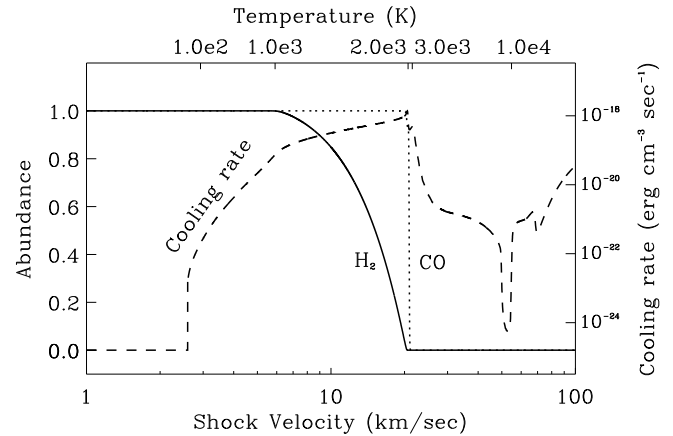

FIG. 18.—Total cooling rate and the abundance of H$_2$ and CO as a function of shock velocity. The initial density before the shock jump is 10^{-21} g cm^{-3}, the temperature 10 K, and the magnetic field 30 μG. The abundances of H$_2$ and CO are normalized to the total amount of H and C, respectively.

0.564 to 3.171t_{cc}, with one run followed all the way to 20.2t_{cc}. For the collapse cases, this gives the total time for the interaction of the shock wave with the molecular cloud core from the initial approach to the triggered collapse of the core. In all cases resulting in the collapse of the system, the timescale is less than two cloud-crushing times. Therefore, the collapse occurs before the RT and KH instabilities usually responsible for the destruction of the cloud have had a chance to establish themselves and tear the core apart. In this sense, our results agree with the calculations of Nittman et al. (1982) and Boss (1995).

The impact of the shock wave pushes the cores into motion in the postshock flow. The fragments in the destroyed cores will eventually be accelerated close to the postshock velocity (KMC). However, for the cases resulting in the triggered collapse of the core, the final velocity of the system can be much lower. The final velocities of the triggered cores listed in Table 2 range from 0.0649 to 4.383 km s^{-1}, with an average value of 1.827 km s^{-1}. The range of velocities of triggered young stellar objects can be expected to vary from ~ 0.01 to a few km s^{-1}, with the result obviously depending on the triggering shock velocity and the preimpact state of the core (radius and density). These velocities are in the same range as the velocity dispersion (0.5–2 km s^{-1}) measured for the T Tauri stars in Taurus-Auriga (Hartmann et al. 1986; Gomez et al. 1993).

The rotation of the cores was not observed to have a noticeable effect on the outcome of the simulations. However, since we did not vary the rotation rate or the orientation of the rotation axis with the direction of the shock wave, further work examining this part of the problem is required.

The last column in Table 2 gives the fraction of the original core mass taking part into collapse. Typically, about $\frac{1}{3}$ of the original core mass is collapsing to form the stellar system, while the rest has been swept downstream. The fraction is larger for the massive cores (runs I and J), which are triggered into collapse rapidly, before most of the core material has been eroded by the shock flow. The efficiency of triggered star formation implied by these results is therefore $\sim 30\%$, possibly even higher for more massive cores. This result agrees well with the observations of the star
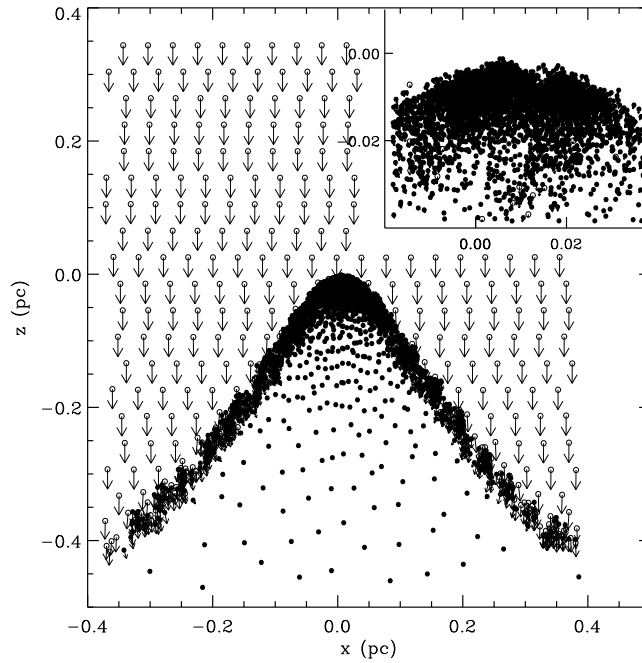
FIG. 19.—Result from a simulation run leading to the formation of a binary system. The system has 20,000 particles in the core and 9000 in the shock wave. The compressed core has fragmented in two pieces, which are collapsing. The peak density in the primary core is 2.28×10^{-9} g cm^{-3}, and in the secondary 8.76×10^{-15} g cm^{-3}. The density in the primary is 3×10^9 times the original core density. The system is shown in the (x, z)-plane at $t = 1.28 \times 10^5$ yr at full scale (*main picture*) and zoomed into the binary (*insert*).

formation efficiencies of high-mass cores in the L1630 molecular cloud (Lada, Evans, & Falgarone 1997).

3.5. *Formation of Binaries*

An unexpected result from our three-dimensional SPH simulations is the triggered collapse resulting in the formation of a multiple star system. These cases are identified in Table 2 in the column labeled "multiple." Figure 19 shows the result of a simulation run (run I) leading to the formation of a binary system. In this particular case, collapse is triggered early during the interaction between the shock wave and the molecular cloud core. The density profile in the line connecting the two cores (Fig. 20) confirms the binary nature of the system. The mass of the primary (right-hand side clump in Fig. 19) and the secondary (left) are 1.67 and 1.52 solar masses, respectively.
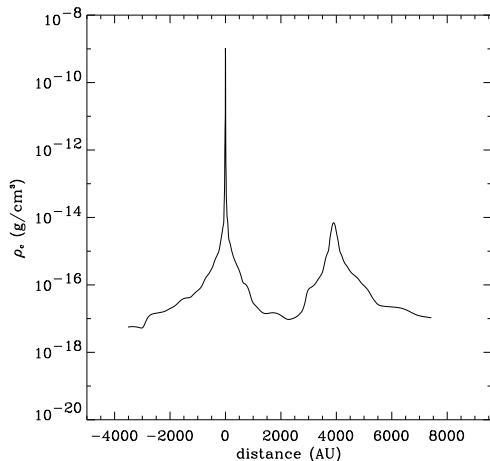

FIG. 20.—Density profile along the line connecting the two fragments in the collapse leading to the formation of a binary system (Fig. 19).

Whether the triggered collapse results in the formation of a single star or a multiple system depends on the evolutionary state of the preimpact core. Since the cores are assumed to have evolved to their preimpact state via ambipolar diffusion, the magnitude of the initial density peak is tied together with the radius and the magnetic flux of the core. In well-evolved cores the central density peak is high and the radius is small at the time of impact. In this case, the result is the collapse of a single mass concentration. If the core is weakly evolved, however, the maximum density in the core is smaller and the radius larger. Upon impact, the compressed system may fragment and form multiple centers of collapse.

The exact condition separating the formation of a multiple system from the collapse to a single object depends on the details of the system, such as the shock velocity and the mass contained in the core. The exploration of the parameter space for the formation of the binary systems is currently under way and will be the subject of a future paper.

4. DISCUSSION

4.1. *Sources of Shocks*

The simulations described in the previous sections employ planar, steady state shock waves, and they do not make any assumptions about their origin. The main results—the possibility of triggered collapse with shock waves with velocities of 20–45 km s^{-1} (and in some cases with velocities as low as 10 km s^{-1}) are applicable to any interstellar shock wave, regardless of its source.

There are several events capable of creating shocks with velocities in the benevolent range. Supernova explosions occurring in the immediate vicinity of molecular clouds are highly destructive, but as the expansion wave encounters ambient matter, it slows down (e.g., Draine & McKee 1993). Assuming an average cloud density of 1000 cm^{-3}, CVH

calculated that the shock wave slows down to velocities of 20–45 km s^{-1} after traveling 3–5 pc, depending on the mass of the supernova. An evolved star entering the asymptotic giant branch phase of its evolution near a molecular cloud can send a shock into the cloud by ejecting a planetary nebula (Cameron 1993; Wasserburg et al. 1994). Nova eruptions close to the cloud are also a possibility (Gehrz, Truran, & Williams 1993). Protostellar outflows are a very attractive source of shocks, since they occur naturally in star formation regions and have velocities in the range 10–100 km s^{-1} (Lada 1985; Fukui et al. 1993), The resulting shocks can therefore either disrupt the evolution of neighboring molecular cloud cores if they are encountered at high velocities or trigger them into collapse if the impact velocity is sufficiently small. Another possible source of shocks in interstellar space is the ultraviolet radiation from hot massive stars, which may ionize nearby cloud material and accelerate gas to the sound speed of ionized hydrogen, ~ 10 km s^{-1} (Elmegreen & Lada 1977).

4.2. The Triggered Origin of the Solar System

An immediate application of our results is the proposal for the triggered origin of the solar system. Our calculations confirm that the impact of an interstellar shock wave can trigger the collapse of a molecular cloud core. However, our calculations do not in general show evidence for the injection of shock wave material into the collapsing system. At the velocities required to trigger collapse, the temperature in the postshock gas is several thousand degrees. The hot shocked material is unable to penetrate deep into the cold, dense core because of buoyancy and entropy effects, and large-scale mixing is therefore prohibited. However, fluid instabilities at the interface between the core and the shocked material bubble trying to penetrate into it will undoubtedly induce dynamically driven mixing, but at scales our three-dimensional calculations are unable to resolve.

KMC have shown that the RT and KH instabilities created during the interaction of the shock wave with the molecular cloud extend all the way to very small scales, and Foster & Boss (1997) and Boss & Foster (1998) have shown that injection is indeed achieved through RT-like fingers. As described in § 3.1, we are able to reproduce the injection efficiency detected by the two-dimensional PPM calculations with our three-dimensional code using an isothermal equation of state. Unlike in the calculations using our full equation-of-state solver, the shock temperature in the comparison runs was lower and the shock thickness smaller, and the material can penetrate into the core in the manner described by Foster & Boss (1997). This suggests that the probability of injection depends on the details of the shock wave, especially the postshock temperature, the thickness of the shock front, and the properties of the postshock flow. Higher resolution studies employing both an isothermal equation of state and variable γ thermodynamics are currently under way.

The time required for the triggered collapse is well within the constraints set by the short-lived radioactivities. From the time the shock wave reaches the nominal core radius of 0.15 pc to the end of the run, the elapsed time is less than 100,000 yr, typically $\sim 57,000$ yr. Combined with the transport time from, for example, a supernova explosion (CVH), this results in the interval from the production of radioactivities to the end of core collapse in less than 150,000 yr, the

mean life of ^{41}Ca (Srinivasan, Ulyanov, & Goswami 1994). Based on both the ease of the induced collapse and the short timescale of the process, our results confirm the viability of the triggered collapse scenario. However, details of the proposal such as the injection of radioactivities, require further work.

4.3. Comparison with Observations

In § 1 we described a few objects where triggered collapse is observed. One of these cases is especially interesting in light of our results. The NICMOS observations of six young stellar objects (YSOs) around a B2 star in the Cone Nebula in Monoceros (Thompson et al. 1998) appears to be a good example of induced collapse. Energetic winds from the B2 star have carved out a cavity in the molecular cloud core in which the star was formed. At some point, the material at the edge of the cavity became gravitationally unstable and collapsed to form the low-mass YSOs observed. Using probable physical properties of the system—an estimate of the mass loss as $10^{-4} M_\odot$ yr^{-1} and assuming a density of $\sim 10^8$ cm^{-3} at the center of the original core—the velocity of the wind at the distance of the YSOs (≈ 4000 AU) is 10–25 km s^{-1}, typical of the simulations we have presented here. The triggered formation of these stars appears to be analogous to the cases where the shock wave impacts cores with low density contrast with the background gas.

4.4. Concerns about Resolution

Truelove et al. (1997) discovered that the numerical noise created by inadequate resolution in grid-based simulations may induce artificial fragmentation in the studies of isothermal collapse of dense molecular cloud cores. They found that in order to avoid this problem, the ratio of the cell size to Jeans length must be kept below 0.25 in the calculations. Bate & Burkert (1997) extended the discussion to the SPH method and found that the resolution requirement is that the minimum resolvable mass in the calculations must be less than the Jeans mass. In practice this means that the smallest Jeans mass encountered during the calculation must be greater than the combined mass of 2 times the number of particles in the SPH kernel.

In the form of the SPH method employed here—where the gravitational softening length and the hydrodynamical smoothing lengths are equal—inadequate resolution would result in inhibiting the collapse and/or the fragmentation of Jeans mass clumps on the scale of the hydrodynamical smoothing length. In order to avoid these resolution problems, we have strived to maintain an adequate number of particles during our simulations. Since we have used equation (11) to keep the number of neighbors between 25 and 60, the resolution requirement for our calculations is that the Jeans mass of a clump of gas must be larger than the combined mass of 50–120 particles. When our calculations progress to the point where the resolution becomes insufficient, we terminate the simulation run.

The question of resolution remains a concern in discussing the details of the problem. As mentioned in the previous sections, our resolution is inadequate to observe the smallest scale Rayleigh-Taylor and Kelvin-Helmholtz instabilities expected to occur at the contact surface between the shock wave and the molecular cloud core. Would it be possible that these small-scale instabilities

could destroy the core even when the large-scale insta-
bilities (which our calculations do resolve) do not? We do
not suspect this to be the case for the following reasons.
According to our studies, the collapse is triggered in less
than two cloud-crushing times, usually even faster. Accord-
ing to the calculations of KMC as well as our failed collapse
cases, the clouds are destroyed after several cloud-crushing
times. Any instabilities present at the core-shock flow
surface during the collapse are not expected to be able to
stop the collapse, but will only mix material from the shock
flow into the core, as suggested by the calculations of Foster
& Boss (1997) or our own isothermal test cases (§ 3.1). If the
small-scale instabilities were able to destroy the cores alone,
without the help of the larger scale instabilities, the destruc-
tion time would be even longer than the timescales dis-
cussed by KMC. We therefore expect the resolution of our
calculations to be sufficient to differentiate between the
cases leading to collapse from those in which the core is
destroyed.

4.5. *Notes on the Assumptions Made in the Calculations*

One of the most important aspects of our simulations is
the crucial role thermodynamics is found to play in the
results. The importance of thermodynamics in the context
of star formation is well known, and there are several
studies examining the collapse and fragmentation of inter-
stellar clouds under nonisothermal conditions (e.g., Low &
Lynden-Bell 1976; Silk 1977; Smith 1980; Tohline 1981;
Whitworth 1981; Hunter & Fleck 1982; Boss 1986;
Tohline, Bodenheimer, & Christodoulou 1987). The main
result of these calculations is that the stability of the clouds
depends on the adiabatic exponent. More specifically, the
usual stability criterion ($\gamma > 4/3$) for adiabatic oscillations
holds for the interstellar clouds, i.e., the clouds become
gravitationally unstable and can also fragment when the
adiabatic exponent falls below $\gamma = 4/3$ (Low & Lynden-Bell
1976; Tohline 1981; Whitworth 1981). The calculations also
stress the importance of cooling in determining the stability
of the clouds (Low & Lynden-Bell 1976; Silk 1977; Tohline
et al. 1987) and discuss the role that initial velocity fields
(e.g., implosion, turbulence, cloud collisions) may play in
reducing the Jeans mass of the clouds and inducing star
formation (Hunter 1979; Smith 1980; Hunter & Fleck
1982). The calculations even suggest that there may be a
range of velocities beneficial for inducing star formation:
higher implosion velocities were found to trigger collapse
when lower velocities failed to do so (Hunter 1979), while a
higher velocity limit for successful development of gravita-
tional instability was suggested by the cloud-cloud collision
calculations (Smith 1980). Combined, these results are
similar to what we have described in § 3.4. Our calculations
confirm the expectation that molecular cloud cores become
gravitationally unstable when the value of the adiabatic
exponent γ falls below 4/3. In typical molecular cloud cores
($T = 10$ K), the value of the adiabatic exponent $\gamma = 5/3$ (see
Fig. 1). In order for the cores to be induced to collapse, the
temperature needs to be raised so that γ falls below the
collapse neutral value. According to the equation of state
used in our calculations, this occurs at $T \approx 27$ K (CVH).
However, it must noted that we have assumed an equi-
librium mix between the ortho and para states of hydrogen
in our calculations, and it is uncertain how well founded
this assumption is. The question of the transformation rates
between the two states of hydrogen has been extensively

discussed in the context of planetary atmospheres (e.g.,
Smith & Gierasch 1995 and references therein). Recent mea-
surements of the ortho-para ratio in interstellar space tend
to confirm the validity of our assumption of an equilibrium
mix (Smith, Davis, & Lioure 1997 and references therein).
However, the distribution between the ortho and para
states may vary in different environments, since the trans-
formation rates depend on the presence of such catalysts as
energetic photons, paramagnetic sites on interstellar grains,
energetic particles, neutral hydrogen atoms, and H_2 mol-
ecules themselves. Studies of the behavior of the ortho-para
ratio in shocks (Timmermann 1998) indicate that the equi-
librium value is quickly reached in shocks with velocities
larger than 20–25 km s^{-1}, while in shocks with lower
speeds the ratio may not deviate much from its preshock
value. The sensitivity of our results to the thermodynamic
conditions stress the need for a more thorough investigation
of this aspect of the problem.

Another key assumption of our calculations is the struc-
ture of the shock wave. Using the conventional approach of
a planar, steady state shock wave (e.g., Draine & McKee
1993) is useful because it does not make any assumptions
about the origin of the shock wave or the behavior of the
medium through which it is traveling. The results are there-
fore applicable to any situation where shocks of the studied
velocity are impacting molecular cloud cores of the
assumed configuration. However, in a more realistic
approach, if the source of the shock wave is nearby, the
shock is not planar but has a radius of curvature. For
example, protostellar outflows are usually observed to form
bow shocks while propagating into the surrounding
medium (Fukui et al. 1993). The inhomogeneities in the
interstellar medium also affect the nature of the shock wave:
in encountering clumps, filaments, holes, tunnels, and
various other observed features of the molecular clouds
(e.g., Pérault, Falgarone, & Puget 1985; Scalo 1985; Bally et
al. 1987; Falgarone & Pérault 1988), the shock wave can be
expected to deviate from the basic planar structure. The
effect of more realistic shock structures on triggered col-
lapse is currently being examined.

5. CONCLUSIONS

The basic conclusions of our three-dimensional SPH cal-
culations of an interstellar shock wave impacting a molecu-
lar cloud core follow:

1. The impact of the shock wave can trigger the collapse
of a molecular cloud core if the shock velocity is 20–45 km
s^{-1}. At higher velocities the core is shredded to pieces by
the instabilities at the contact surface between the core and
the shock wave. At lower velocities, the core is usually not
compressed sufficiently for self-gravity to be able to over-
come the disruptive effect of instabilities.

2. Thermodynamics plays a crucial role in determining
the result: in order for the compressed core to collapse, the
value of the adiabatic exponent in the core material needs to
fall below 4/3. In typical molecular cloud conditions this
occurs at the temperature of approximately 27 K.

3. The critical velocity of 20 km s^{-1} required for trig-
gered collapse arises from the cooling function in the post-
shock gas: at higher velocities the principal coolants CO
and H_2 are destroyed, the postshock gas remains hot and
sufficient gas pressure is exerted on the core to drive it into

collapse. At lower velocities the molecular coolants survive, the postshock gas is cooled efficiently, and the pressure is insufficient to trigger collapse.

4. The evolutionary state of the preimpact core influences the outcome: highly evolved cores can be triggered to collapse even at low shock velocities. Weakly evolved cores may fragment during compression and form binaries.

REFERENCES

Bally, J., Langer, W. D., Stark, A. A., & Wilson, R. W. 1987, ApJ, 312, L45
Bate, M. R., & Burkert, A. 1997, MNRAS, 288, 1060
Bedogni, R., & Woodward, P. R. 1990, A&A, 231, 481
Benz, W. 1990, in The Numerical Modelling of Nonlinear Stellar Pulsations, ed. J. R. Buchler (Dordrecht: Kluwer), 269
Benz, W., Bowers, R. L., Cameron, A. G. W., & Press, W. H. 1990, ApJ, 348, 647
Boss, A. P. 1986, ApJS, 62, 519
———. 1995, ApJ, 439, 224
Boss, A. P., & Foster, P. N. 1997, in Astrophysical Implications of the Laboratory Study of Presolar Materials, ed. T. J. Bernatowicz & E. Zinner (Woodbury: AIP), 649
———. 1998, ApJ, 494, L103
Burgess, A., & Seaton, M. J. 1960, MNRAS, 120, 121
Cameron, A. G. W. 1993, in Protostars and Planets III, ed. E. H. Levy & J. I. Lunine (Tucson: Univ. Arizona Press), 47
Cameron, A. G. W., Höflich, P., Myers, P. C., & Clayton, D. D. 1995, ApJ, 447, L53
Cameron, A. G. W., & Truran, J. W. 1977, Icarus, 30, 447
Cameron, A. G. W., Vanhala, H., & Höflich, P. 1997, in Astrophysical Implications of the Laboratory Study of Presolar Materials, ed. T. J. Bernatowicz & E. Zinner (Woodbury: AIP), 665 (CVH)
Chackerian, Jr., C., & Tipping, R. H. 1983, J. Mol. Spectrosc., 99, 431
Chen, H., Tokunaga, A. T., Strom, K. M., & Hodapp, K.-W. 1993, ApJ, 407, 639
Clayton, D. D., & Jin, L. 1995a, ApJ, 451, 681
———. 1995b, ApJ, 451, L87
Crutcher, R. M., Troland, T. H., Goodman, A. A., Heiles, C., Kazès, I., & Myers, P. C. 1993, ApJ, 407, 175
Cunto, W., & Mendoza, C. 1992, TOPBASE 0.7, IBM Venezuela Scientific Center
DeCampli, W. M., Cameron, A. G. W., Bodenheimer, P., & Black, D. C. 1978, ApJ, 223, 854
Draine, B. T., & McKee, C.F. 1993, ARA&A, 31, 373
Elmegreen, B. G. 1990, ApJ, 361, L77
———. 1998, in Origins of Galaxies, Stars, Planets and Life, ed. C. E. Woodward, J. M. Shull, & H. A. Thronson, Jr. (San Francisco: ASP), 150
Elmegreen, B. G., & Lada, C. J. 1977, ApJ, 214, 725
Falgarone, E., & Pérault, M. 1988, A&A, 205, L1
Flower, D. R., Pineau-des-Forets, G., & Hartquist, T. W. 1986, MNRAS, 218, 729
Foster, P. N., & Boss, A. P. 1996, ApJ, 468, 784 (FB96)
———. 1997, ApJ, 489, 346
Fukui, Y., Iwata, T., Mizuno, A., Bally, J., & Lane, A. P. 1993, in Protostars and Planets III, ed. E. H. Levy & J. I. Lunine (Tucson: Univ. Arizona Press), 603
Gayet, R. 1970, A&A, 9, 312
Gehrz, R. D., Truran, J. W., & Williams, R. E. 1993, in Protostars and Planets III, ed. E. H. Levy & J. I. Lunine (Tucson: Univ. Arizona Press), 75
Gomez, M., Hartmann, L., Kenyon, S. J., & Hewett, R. 1993, AJ, 105, 1927
Graham, J. A. 1998, ApJ, 502, 245
Graham, J. A., & Elias, J. H. 1983, ApJ, 272, 615
Graham, J. A., & Heyer, M. H. 1989, PASP, 101, 573
Hartmann, L., Hewett, R., Stahler, S., & Mathieu, R. D. 1986, ApJ, 309, 275
Heathcote, S. R., & Brand, P. W. J. L. 1983, MNRAS, 203, 67
Herant, M. 1994, Mem. Soc. Astron. Ital., 65, 1013
Herbst, W., & Assousa, G. E. 1977, ApJ, 217, 473
Herzberg, G. 1967, Molecular Spectra and Molecular Structure I. Spectra of Diatomic Molecules (Princeton: Van Nostrand)
Hester, J. J., et al. 1991, ApJ, 369, L75
———. 1996, AJ, 111, 2349
Higdon, J. L., & Wallin, J. F. 1997, ApJ, 474, 686
Höflich, P., Khokhlov, A. M., & Wheeler, J. C. 1995, ApJ, 444, 831
Höflich, P., Müller, E., & Khokhlov, A. 1993, A&A, 268, 570
Hollenbach, D., & McKee, C. F. 1979, ApJS, 41, 555
Hunter, Jr., J. H. 1979, ApJ, 233, 946
Hunter Jr., J. H., & Fleck Jr., R. C. 1982, ApJ, 256, 505
Klein, R. I., McKee, C. F., & Colella, P. 1994, ApJ, 420, 213 (KMC)
Krebs, J., & Hillebrandt, W. 1983, A&A, 128, 411

Kurucz, R. L. 1991, CD-ROM 1 (Cambridge: Center for Astrophysics)
Lada, C. J. 1985, ARA&A, 23, 267
Lada, C. J., & Lada, E. A. 1991, in The Formation and Evolution of Star Clusters, ed. K. Jones (San Francisco: ASP), 3
Lada, E. A., Evans, N. J. II, & Falgarone, E. 1997, ApJ, 488, 286
Lang, K. R. 1980, Astrophysical Formulae (Berlin: Springer)
Low, C., & Lynden-Bell, D. 1976, MNRAS, 176, 367
Mac Low, M.-M., McKee, C. F., Klein, R. I., Stone, J. M., & Norman, M. L. 1994, ApJ, 433, 757
McKee, C. F., Zweibel, E. G., Goodman, A. A., & Heiles, C. 1993, in Protostars and Planets III, ed. E. H. Levy & J. I. Lunine (Tucson: Univ. Arizona Press), 327
Monaghan, J. J. 1992, ARA&A, 30, 543
Mouschovias, T. Ch. 1989, in The Physics and Chemistry of Interstellar Molecular Clouds, ed. G. Winnewasser & J. T. Armstrong (Berlin: Springer), 297
———. 1991, ApJ, 373, 169
Nittman, J., Falle, S. A. E. G., & Gaskell, P. H. 1982, MNRAS, 201, 833
O'Dell, C. R., & Wen, Z. 1994, ApJ, 436, 194
O'Dell, C. R., Wen, Z., & Hu, X. 1993, ApJ, 410, 696
Osterbrock, D. E., & O'Dell, C. R., eds. 1968, Planetary Nebulae (Dordrecht: Reidel)
Peach, G. 1967, MmRAS, 71, 1
Pérault, M., Falgarone, E., & Puget, J. L. 1985, A&A, 152, 371
Podosek, F. A., & Nichols Jr., R. H. 1997, in Astrophysical Implications of the Laboratory Study of Presolar Materials, ed. T. J. Bernatowicz & E. Zinner (Woodbury: AIP), 617
Reilman, R. F., & Manson, S. T. 1979, ApJS, 40, 815
Różyczka, M., & Tenorio-Tagle, G. 1987, A&A, 176, 329
Ruzmaikina, T. V., & Ip, W. H. 1994, Icarus, 112, 430
Scalo, J. M. 1985, in Protostars and Planets II, ed. D. C. Black & M. S. Matthews (Tucson: Univ. Arizona Press), 201
Schwartz, R. D. 1977, ApJ, 212, L25
Seaton, M. J. 1960, Rep. Prog. Phys., 23, 313
Shu, F. H. 1995, in Molecular Clouds and Star Formation, ed. Chi Yuan & Junhan You (Singapore: World Scientific), 97
Shu, F. H., Adams, F. C., & Lizano, S. 1987, ARA&A, 25, 23
Shu, F. H., Shang, H., Glassgold, A.E., & Lee, T. 1997, Science, 277, 1475
Shu, F. H., Shang, H., & Lee, T. 1996, Science, 271, 1545
Silk, J. 1977, ApJ, 214, 152
Smith, J. 1980, ApJ, 238, 842
Smith, M. D., Davis, C. J., & Lioure, A. 1997, A&A, 327, 1206
Smith, M. D., & Gierasch, P. J. 1995, Icarus, 116, 159
Srinivasan, G., Ulyanov, A. A., & Goswami, J. N. 1994, ApJ, 431, L67
Stone, J. M., & Norman, M. L. 1992, ApJ, 390, L17
Swings, J.-P., ed. 1988, Trans. IAU, Vol. XXA (Dordrecht: Kluwer), 111
Thompson, R. I., Corbin, M. R., Young, E., & Schneider, G. 1998, ApJ, 492, L177
Timmermann, R. 1998, ApJ, 498, 246
Tohline, J. E. 1981, ApJ, 248, 717
Tohline, J. E., Bodenheimer, P. H., & Christodoulou, D. M. 1987, ApJ, 322, 787
Troland, T. H., Crutcher, R. M., Goodman, A. A., Heiles, C., Kazès, I., & Myers, P. C. 1996, ApJ, 471, 302
Truelove, J. K., Klein, R. I., McKee, C. F., Holliman II, J. H., Howell, L. H., & Greenough, J. A. 1997, ApJ, 489, L179
Turner, J., Kirby-Docken, K., & Dalgarno, A. 1977, ApJS, 35, 281
Vanhala, H. 1993, Ap&SS, 204, 129
Walter, F. M., Vrba, F. J., Mathieu, R. D., Brown, A., & Myers, P. C. 1994, AJ, 107, 692
Wasserburg, G. J., Busso, M., Gallino, R., & Raiteri, C. M. 1994, ApJ, 424, 412
Wasserburg, G. J., Gallino, R., Busso, M., Goswami, J. N., & Raiteri, C. M. 1995, ApJ, 440, L101
Wayman, P. A., ed. 1982, Trans. IAU, Vol. XVIIIA (Dordrecht: Kluwer), 115
West, R. M., ed. 1985, Trans. IAU, Vol. XIXA (Dordrecht: Kluwer), 121
Whitworth, A. 1981, MNRAS, 195, 967
Woodward, P. R. 1976, ApJ, 207, 484
Xu, J., & Stone, J. M. 1995, ApJ, 454, 172